Prepared for submission to JHEP

The hadronic vacuum polarization contribution to the muon $g-2$ at long distances

Dalibor Djukanovic,[a,b] **Georg von Hippel,**[c] **Simon Kuberski,**[d] **Harvey B. Meyer,**[c,a,b] **Nolan Miller,**[a,b] **Konstantin Ottnad,**[c] **Julian Parrino,**[c] **Andreas Risch,**[e] **Hartmut Wittig**[c,a,b]

[a] *Helmholtz-Institut Mainz, Johannes Gutenberg-Universität Mainz, 55099 Mainz, Germany*
[b] *GSI Helmholtz Centre for Heavy Ion Research, 64291 Darmstadt, Germany*
[c] *PRISMA+ Cluster of Excellence and Institut für Kernphysik, Johannes Gutenberg-Universität Mainz, 55099 Mainz, Germany*
[d] *Theoretical Physics Department, CERN, 1211 Geneva 23, Switzerland*
[e] *Department of Physics, University of Wuppertal, Gaussstr. 20, 42119 Wuppertal, Germany*

E-mail: simon.kuberski@cern.ch

Abstract: We present our lattice QCD result for the long-distance part of the hadronic vacuum polarization contribution, $(a_\mu^{\rm hvp})^{\rm LD}$, to the muon $g-2$ in the time-momentum representation. This is the numerically dominant, and at the same time the most challenging part regarding statistical precision. Our calculation is based on ensembles with dynamical up, down and strange quarks, employing the $\mathrm{O}(a)$-improved Wilson fermion action with lattice spacings ranging from $0.035-0.099\,\mathrm{fm}$. In order to reduce statistical noise in the long-distance part of the correlator to the per-mille level, we apply low-mode averaging and combine it with an explicit spectral reconstruction. Our result is $(a_\mu^{\rm hvp})^{\rm LD} = 423.2(4.2)_{\rm stat}(3.4)_{\rm syst}\times 10^{-10}$ in isospin-symmetric QCD, where the pion decay constant is used to set the energy scale. When combined with our previous results for the short- and intermediate-distance window observables and after including all sub-dominant contributions as well as isospin-breaking corrections, we obtain the total leading-order hadronic vacuum polarization contribution as $a_\mu^{\rm hvp} = 724.9(5.0)_{\rm stat}(4.9)_{\rm syst}\times 10^{-10}$. Our result displays a tension of 3.9 standard deviations with the data-driven estimate published in the 2020 White Paper, but leads to a SM prediction for the total muon anomalous magnetic moment that agrees with the current experimental average.

CERN-TH-2024-196, MITP-24-080

Contents

1 Introduction

For many years the tension between the experimentally measured muon anomalous magnetic moment $a_\mu \equiv \frac{1}{2}(g-2)_\mu$ and its theoretical prediction has been one of the most promising hints for physics beyond the Standard Model. The largest share of the uncertainty in the Standard Model prediction arises through the leading-order hadronic vacuum polarization (HVP) contribution, $a_\mu^{\rm hvp}$. In the traditional data-driven method, which forms the basis for the consensus value reported in the 2020 White Paper by the Muon $g-2$ Theory Initiative [1], one obtains $a_\mu^{\rm hvp}$ from a dispersion integral over the experimentally measured hadronic cross section, $e^+e^- \to$ hadrons [2–7]. However, since the publication of the White Paper, this approach has been challenged on two fronts (see, e.g., [8, 9]): Firstly, the cross section for the dominant channel $e^+e^- \to \pi^+\pi^-$ measured recently by CMD-3 [10, 11] is significantly enhanced relative to all other experiments, yielding an estimate for $a_\mu^{\rm hvp}$ that is largely compatible with the latest direct measurement of a_μ reported by the E989 experiment [12, 13]. Secondly, lattice QCD calculations have produced precise results for $a_\mu^{\rm hvp}$ [14] and the so-called intermediate window observable $(a_\mu^{\rm hvp})^{\rm ID}$ [14–21] indicating a strong tension with estimates derived from e^+e^- cross sections published prior to CMD-3. Tracing the origin(s) of these tensions and their possible resolution is the subject of intense research.

In this paper, we report the results of a new precision calculation of $a_\mu^{\rm hvp}$ in lattice QCD. The main ingredient, which we describe in full detail in the following sections, is the fully blinded calculation of the long-distance window observable $(a_\mu^{\rm hvp})^{\rm LD}$ in isospin-symmetric QCD (isoQCD), for which we obtain

$$(a_\mu^{\rm hvp})^{\rm LD} = (423.2 \pm 4.2_{\rm stat} \pm 3.4_{\rm syst}) \times 10^{-10}\,. \tag{1.1}$$

When combined with our previous results for the short- and intermediate-distance window observables [18, 22], we obtain the total light-quark connected contribution as

$$(a_\mu^{\rm hvp})^{ud,\,{\rm conn}} = (675.7 \pm 4.1_{\rm stat} \pm 3.7_{\rm syst}) \times 10^{-10}\,, \tag{1.2}$$

which disagrees with the corresponding data-driven evaluation [23] by more than five standard deviations. After including all sub-leading contributions and accounting for isospin-breaking corrections we finally arrive at

$$a_\mu^{\rm hvp} = (724.9 \pm 5.0_{\rm stat} \pm 4.9_{\rm syst}) \times 10^{-10}\,. \tag{1.3}$$

This result differs from the White Paper estimate for $a_\mu^{\rm hvp}$ by 3.9 standard deviations, whilst being compatible with the current experimental average for a_μ. It is also higher than the lattice estimate by the BMW collaboration [14], as well as their recent update [24], which partly relies on the data-driven method.

This paper is organized as follows: In section 2 we describe the details of our calculation, including our noise-reduction strategy, the extrapolation to the physical point and the determination of finite-volume corrections. Our main results are presented in section 3, including the long-distance window observables and the total HVP contribution in isospin-symmetric QCD, as well as the correction for isospin-breaking effects that must be added to arrive at our final result for $a_\mu^{\rm hvp}$. After presenting our conclusions, we discuss additional computational details in several appendices, including our choice of hadronic scheme (appendix A), our blinding strategy (appendix B), the use of low-mode averaging as noise-reduction strategy (appendix C) and the spectral reconstruction of the long-distance tail of the vector correlator (appendix D). Detailed results for the long-distance contributions and ancillary information on individual ensembles are collected in appendix E.

2 Setup

2.1 Basic definitions

We employ the standard time-momentum representation (TMR) [25] to express the HVP contribution $a_\mu^{\rm hvp}$ as the Euclidean time integral of the spatially summed correlator $G(t)$ of the electromagnetic current, J_μ^γ, convoluted with an analytically known kernel function, i.e.

$$a_\mu^{\rm hvp} = \left(\frac{\alpha}{\pi}\right)^2 \int_0^\infty dt\, \tilde{K}(t;\, m_\mu) G(t)\,, \quad \delta_{kl} G(t) = -\int d^3x\, \left\langle J_k^\gamma(t,\boldsymbol{x}) J_l^\gamma(0) \right\rangle \tag{2.1}$$

$$J_\mu^\gamma = \frac{2}{3}\bar{u}\gamma_\mu u - \frac{1}{3}\bar{d}\gamma_\mu d - \frac{1}{3}\bar{s}\gamma_\mu s + \frac{2}{3}\bar{c}\gamma_\mu c + \ldots\,. \tag{2.2}$$

The electromagnetic current can be written conveniently with the help of matrices T^m acting in flavour space. Adopting the notation

$$J_\mu^m \equiv \overline{\psi}\, T^m \gamma_\mu\, \psi, \qquad \overline{\psi} = (\bar{u},\, \bar{d},\, \bar{s},\, \bar{c},\, \bar{b}) \tag{2.3}$$

we describe the $(u,\, d,\, s)$ flavour sector by setting

$$T^m = \tfrac{1}{2}\lambda^m \oplus \mathbf{0}, \quad m = 1, \ldots, 8\,, \tag{2.4}$$

where λ^m denote the Gell-Mann matrices, and $\mathbf{0}$ the null matrix of size 2×2. The charm and bottom quark currents are defined by $T^{\rm c} = {\rm diag}(0,\,0,\,0,\,1,\,0)$ and $T^{\rm b} = {\rm diag}(0,\,0,\,0,\,0,\,1)$, respectively. The generic correlator $G^{(m,\,n)}$ of the currents J_μ^m and J_μ^n is then given by

$$\delta_{kl} G^{(m,\,n)}(t) = -\int d^3x\, \langle J_k^m(t,\boldsymbol{x}) J_l^n(0)\rangle\;. \tag{2.5}$$

Setting $m = \gamma$ corresponds to identifying T^m with the physical quark charge matrix, i.e. $T^\gamma = {\rm diag}(\frac{2}{3},\, -\frac{1}{3},\, -\frac{1}{3},\, \frac{2}{3},\, -\frac{1}{3})$, which yields the following decomposition of the electromagnetic current correlator $G(t) \equiv G^{(\gamma,\,\gamma)}(t)$:

$$G^{(\gamma,\gamma)} = G^{(3,3)} + \frac{1}{3}G^{(8,8)} + \frac{4}{9}G^{(\rm c,c)}_{\rm conn} + \frac{2}{3\sqrt{3}}G^{(\rm c,8)} + \frac{4}{9}G^{(\rm c,c)}_{\rm disc} + \frac{1}{9}G^{(\rm b,b)}_{\rm conn} + \ldots\,. \tag{2.6}$$

Here the subscripts denote the quark-connected and -disconnected contributions, and the ellipsis stands for contributions too small to be relevant in this work. Correspondingly, we can define separate TMR integrals for each correlator $G^{(m,n)}$ as

$$a_\mu^{m,n} = \left(\frac{\alpha}{\pi}\right)^2 \int_0^\infty dt\, \tilde{K}(t;\, m_\mu) G^{(m,n)}(t)\,. \tag{2.7}$$

In this way, we recover the isovector contribution as $a_\mu^{3,3}$, while the isoscalar contribution is given by $\frac{1}{3}a_\mu^{8,8}$.

Our focus in this paper is the long-distance window observable, $(a_\mu^{\rm hvp})^{\rm LD}$, first defined in ref. [26], which is obtained by multiplying the integrand in eq. (2.1) with an additional factor $\Theta(t,\, d_1,\, \Delta)$:

$$(a_\mu^{\rm hvp})^{\rm LD} = \left(\frac{\alpha}{\pi}\right)^2 \int_0^\infty dt\, \tilde{K}(t;\, m_\mu)\, G(t)\, \Theta(t,\, d_1,\, \Delta)\,, \tag{2.8}$$

where

$$\Theta(t,\, d_1,\, \Delta) = \tfrac{1}{2}\,(1 + \tanh[(t - d_1)/\Delta]) \tag{2.9}$$

is a smoothed step function at $t \approx d_1$ with width Δ. With this convention the standard long-distance window is defined for $d_1 = 1.0\,\text{fm}$ and $\Delta = 0.15\,\text{fm}$. In the same manner we identify the long-distance window observables for the flavour decomposition as

$$(a_\mu^{m,n})^{\rm LD} = \left(\frac{\alpha}{\pi}\right)^2 \int_0^\infty dt\, \tilde{K}(t;\, m_\mu)\, G^{(m,n)}(t)\, \Theta(t,\, d_1,\, \Delta)\,. \tag{2.10}$$

For completeness, we list the short- and intermediate-distance window observables, i.e.

$$(a_\mu^{\rm hvp})^{\rm SD} = \left(\frac{\alpha}{\pi}\right)^2 \int_0^\infty dt\, \tilde{K}(t;\, m_\mu)\, G(t)\, [1 - \Theta(t,\, d_0,\, \Delta)]\,, \tag{2.11}$$

$$(a_\mu^{\rm hvp})^{\rm ID} = \left(\frac{\alpha}{\pi}\right)^2 \int_0^\infty dt\, \tilde{K}(t;\, m_\mu)\, G(t)\, [\Theta(t,\, d_0,\, \Delta) - \Theta(t,\, d_1,\, \Delta)]\,, \tag{2.12}$$

where the standard choice is $d_0 = 0.4\,\text{fm}$. The generalization of these observables to the flavour decomposition is obvious.

As detailed in appendix B, we have fully blinded our analysis by using five modified versions of the kernel function, which only converge in the continuum limit, differing by a multiplicative factor. After finalizing the analysis, we first performed the unblinding step, and only then switched to the true kernel function, $\tilde{K}(t;\, m_\mu)$, to produce the results and figures presented in this work. In the following, all results for HVP contributions to a_μ are quoted in units of 10^{-10} unless otherwise specified.

2.2 Gauge ensembles

We perform our calculation on a subset of the $2+1$-flavour CLS ensembles [27, 28] which feature a tree-level Symanzik improved Lüscher-Weisz gauge action and non-perturbatively $\mathrm{O}(a)$ improved Wilson quarks [29]. The RHMC algorithm is used to simulate the strange quark component, and a small twist in the Dirac operator stabilizes the simulations of light quark masses in large volumes. The target action, $2+1$-flavour QCD, is restored by the inclusion of the appropriate reweighting factors [30–33]. We focus on the chiral trajectory where the sum of the bare sea quark masses is held constant. Starting from the SU(3) symmetric point where $m_\pi = m_K \approx 420\,\text{MeV}$, the kaon mass approaches its physical value from below when the pion mass is lowered towards its physical value since the combination $m_K^2 + \frac{1}{2}m_\pi^2$ is approximately constant along each chiral trajectory. We also include ensembles with a close-to-physical strange quark mass and pion masses around 220 MeV to stabilize the interpolation to physical quark masses. Three ensembles at physical values of the light quark mass enter our interpolation, thereby allowing us to tightly constrain the chiral behaviour.

Compared to our 2019 computation [34], we have significantly extended the set of gauge ensembles which now covers six lattice spacings from about 0.01 fm down to 0.039 fm. Eight gauge ensembles with pion masses ranging from 225 MeV down to 131 MeV have been added or significantly extended to allow for a safe interpolation to physical quark masses and to constrain possible mass-dependent cutoff effects. Replacing several ensembles with relatively small spatial box sizes by new ensembles with larger volumes greatly strengthens our confidence in controlling finite-size effects, both by reducing the size of the correction and by offering an explicit check that we can quantitatively describe the finite-size effects that are found in the data. Further details concerning the set of ensembles and their inclusion in our work can be found in refs. [18, 22, 34, 35].

2.3 The electromagnetic current on the lattice

We use two different discretizations, i.e. the local (L) and the point-split (C) variant to realize the vector current of eq. (2.3) on the lattice

$$J_\mu^{(\mathrm{L}),a}(x) = \overline{\psi}(x)\gamma_\mu T^a \psi(x)\,, \tag{2.13}$$

$$\begin{aligned} J_\mu^{(\mathrm{C}),a}(x) = \frac{1}{2}\Big(&\overline{\psi}(x+a\hat{\mu})(1+\gamma_\mu)U_\mu^\dagger(x)T^a\psi(x) \\ &- \overline{\psi}(x)(1-\gamma_\mu)U_\mu(x)T^a\psi(x+a\hat{\mu})\Big)\,, \end{aligned} \tag{2.14}$$

where $U_\mu(x)$ is the gauge link in the direction $\hat{\mu}$ associated with site x. With the local tensor current defined as $\Sigma^a_{\mu\nu}(x) = -\frac{1}{2}\,\overline{\psi}(x)[\gamma_\mu,\gamma_\nu]T^a\psi(x)$, we obtain the $\mathrm{O}(a)$-improved versions of the currents via

$$J_\mu^{(\alpha),a,I}(x) = J_\mu^{(\alpha),a}(x) + a c_\mathrm{V}^{(\alpha)}(g_0)\,\partial_\nu \Sigma^a_{\mu\nu}(x)\,, \quad \alpha = \mathrm{L},\,\mathrm{C}\,. \tag{2.15}$$

Employing the non-perturbative determination of the improvement coefficients $c_\mathrm{V}^{(\alpha)}(g_0)$ ensures the removal of cutoff effects of $\mathrm{O}(a)$ in the chiral limit. The line of constant physics (LCP) that is chosen in the formulation and evaluation of the relevant improvement condition is ambiguous regarding higher-order cutoff effects. As a consequence, matrix elements of $\mathrm{O}(a)$-improved currents that differ in the choice of LCP approach the continuum limit with different rates in a^2. In previous works, we have used two alternative sets of non-perturbatively determined coefficients from [38] and [39] and interpreted possible deviations in the continuum limit as systematic uncertainties of the continuum extrapolation.

The calculation of $c_\mathrm{V}^{(\alpha)}(g_0)$ in [38] was based on a preliminary determination of the improvement coefficient $\tilde{b}_\mathrm{A}$ that enters the improvement condition. However, the final results for $\tilde{b}_\mathrm{A}$ published in [40] differ significantly from the preliminary ones used in [38]. In turn, an updated determination of $c_\mathrm{V}^{(\alpha)}(g_0)$ using the published values of $\tilde{b}_\mathrm{A}$ and additional SU(3)-symmetric ensembles [41] yield coefficients that differ significantly from those in [38] while being much closer to the ones extracted directly at vanishing quark masses in the

Id	β	bc	$\left(\frac{L}{a}\right)^3 \times \frac{T}{a}$	a [fm]	m_π [MeV]	m_K [MeV]	$m_\pi L$	L [fm]	MDU
A653	3.34	p	$24^3 \times 48$	0.097	430	430	5.1	2.3	20200
A654		p	$24^3 \times 48$		338	462	4.0	2.3	16000
H101	3.4	o	$32^3 \times 96$	0.085	424	424	5.8	2.7	8064
H102		o	$32^3 \times 96$		358	445	4.9	2.7	7832
H105*		o	$32^3 \times 96$		283	470	3.9	2.7	8260
N101		o	$48^3 \times 128$		282	468	5.8	4.1	6376
C101		o	$48^3 \times 96$		222	478	4.6	4.1	8000
C102†		o	$48^3 \times 96$		224	506	4.6	4.1	6000
D150†		p	$64^3 \times 128$		131	484	3.6	5.4	1616
B450	3.46	p	$32^3 \times 64$	0.075	422	422	5.1	2.4	6448
S400*		o	$32^3 \times 128$		355	447	4.3	2.4	11492
N452		p	$48^3 \times 128$		356	447	6.5	3.6	4000
N451		p	$48^3 \times 128$		291	468	5.3	3.6	4044
D450		p	$64^3 \times 128$		219	483	5.3	4.8	2000
D451†		p	$64^3 \times 128$		219	509	5.3	4.8	3700
D452		p	$64^3 \times 128$		156	490	3.8	4.8	4000
H200*	3.55	o	$32^3 \times 96$	0.064	423	423	4.4	2.0	8000
N202		o	$48^3 \times 128$		417	417	6.4	3.0	7608
N203		o	$48^3 \times 128$		349	447	5.4	3.0	6172
N200		o	$48^3 \times 128$		286	468	4.4	3.0	6848
D251		p	$64^3 \times 128$		286	467	5.9	4.1	5968
D200		o	$64^3 \times 128$		202	486	4.2	4.1	8004
D201†		o	$64^3 \times 128$		202	507	4.2	4.1	4312
E250†		p	$96^3 \times 192$		131	495	4.1	6.1	4496
N300*	3.7	o	$48^3 \times 128$	0.049	425	425	5.1	2.4	8188
J307		o	$64^3 \times 192$		424	424	6.7	3.1	3200
N302*		o	$48^3 \times 128$		350	456	4.2	2.4	8804
J306		o	$64^3 \times 192$		349	455	5.6	3.1	3840
J303		o	$64^3 \times 192$		260	480	4.1	3.1	8584
J304†		o	$64^3 \times 192$		263	530	4.2	3.1	6508
E300		o	$96^3 \times 192$		177	498	4.2	4.7	7180
F300†		o	$128^3 \times 256$		136	496	4.3	6.3	1412
J500	3.85	o	$64^3 \times 192$	0.039	417	417	5.2	2.5	15000
J501		o	$64^3 \times 192$		337	450	4.2	2.5	15680

Table 1. Parameters of the simulations: the bare coupling $\beta = 6/g_0^2$, the temporal boundary conditions, open (o) or anti-periodic (p), the lattice dimensions, the lattice spacing a in physical units based on [36, 37], the approximate pion and kaon masses, the physical size of the lattice and the length of the Monte Carlo chain in Molecular Dynamics Units (MDU). Ensembles with an asterisk are used to control finite-size effects, but are not included in the final analysis. Ensembles marked by a dagger lie on a second chiral trajectory where $m_s \approx m_s^{\rm phys}$. Ensembles in bold face have either been added or the current correlator has been determined with significantly improved precision with respect to [34].

Schrödinger functional scheme employed in [39]. In this work, we will use the updated values of [41] for set 1 and employ them to cross-check our main results which will be computed using the published values of [39] (set 2). We note that our earlier results for the short- and intermediate-distance windows [18, 22] are unaffected by the change of improvement coefficients of set 1.

The renormalization pattern of the electromagnetic current based on Wilson quarks has been outlined in refs. [18, 34, 35], and we use the renormalization factor and improvement coefficients of [38] and [39, 42], respectively, in combination with set 1 and set 2 of improvement coefficients $c_{\mathrm{V}}^{(\alpha)}$. The values of the critical hopping parameters that enter the mass-dependent improvement via the bare subtracted quark mass are taken from [37].

2.4 Noise reduction in the long-distance tail

One of the two main difficulties in the computation of the long-distance contribution to a_μ^{hvp} is the exponential loss of signal in the light-connected and disconnected correlation functions. In this work we employ several advanced noise reduction techniques to enhance the statistical signal, focusing on the light-quark connected correlation function which contributes about 90% of the total a_μ^{hvp}. Specifically, we combine improved estimators from low-mode averaging (LMA) and the spectral reconstruction of the isovector correlation function with the widely used bounding method.

In our previous work [34], the light-quark connected correlation function was computed either from point sources or from time, spin and colour-diluted time slice sources. In both cases, assuming that multiple sources on a gauge configuration are largely uncorrelated, the statistical uncertainty at a certain source-sink separation scales $\propto 1/\sqrt{N}$ with the number of sources N. A brute-force reduction of the statistical error by increasing the number of sources is infeasible in the long-distance regime and at close-to-physical values of the light quark masses, since the signal deteriorates exponentially fast.

In this work, we resort to an improved estimator for the light-connected correlation function that is based on the low modes of the Dirac operator. For small values of the light quark mass, we find low-mode averaging (LMA) [43, 44] to yield significantly more accurate results compared to our old setup, and thus we employ LMA for all ensembles with pion masses smaller than 280 MeV. We refer to appendix C for a detailed explanation of our setup for the LMA computation. Our setup for computing the quark-disconnected correlation functions via a combination of frequency-splitting techniques [45, 46] and hierarchical probing [47] in combination with the generalized hopping parameter expansion [48] has been extensively discussed in appendix C of [35].

Euclidean finite-volume two-point correlation functions at source-sink separation t can be expressed via the spectral decomposition

$$G^{(k,l)}(t) = \sum_{n=0}^{\infty} \frac{Z_n^2}{2E_n}\, \mathrm{e}^{-E_n t}\,, \tag{2.16}$$

where Z_n denote the real amplitudes and E_n the ordered real and positive finite-volume energies. At sufficiently large time separations, only the lowest-lying states contribute significantly, as contributions from higher-energy states decay faster. In this regime, the finite-volume isovector correlation function $G^{(3,3)}(t)$ is dominated by two-pion states. These can be computed in a dedicated spectroscopy study, as outlined in appendix D.

In both the isovector and isoscalar channels, we make use of the representation in eq. (2.16) to impose lower and upper bounds on $G^{(k,l)}(t)$ via [26, 34, 49, 50]

$$0 \leq G^{(k,l)}(t_c)\, \mathrm{e}^{-E^*_{\mathrm{eff}}(t-t_c)} \leq G^{(k,l)}(t) \leq G^{(k,l)}(t_c)\, \mathrm{e}^{-E_0(t-t_c)}\,, \qquad t \geq t_c\,. \tag{2.17}$$

Here, E_0 is the energy level of the lowest-lying state that contributes to the correlation function. In practice, it has to be computed or estimated from the data.

On those ensembles for which we performed a dedicated spectroscopy study in the isovector channel, we employ the lowest state determined from the generalized eigenvalue problem (GEVP). On all other ensembles, we use a Gounaris-Sakurai parameterization of the timelike pion form factor, which is used to compute the finite-volume correction (see section 2.6), to estimate the ground-state energy, which is always found to lie below that of two non-interacting pions. We note that the lowest energy levels determined by the Gounaris-Sakurai fit agree with those from the dedicated spectroscopy study. We use the central value minus the statistical uncertainty of this estimate as input for E_0. As in [35], this estimate for E_0 is also used for the isoscalar correlation function, which is justified by the fact that $m_\rho \lesssim m_\omega$, making this a conservative choice.

The energy E^*_{eff} is determined from the effective mass of the correlation function at some time $t_{\mathrm{eff}} < t_c$, as computed from the logarithmic derivative of the correlation function. In this work, we fix t_{eff} on each ensemble such that the effective mass at this distance is clearly larger than in the region where the bounding method will be applied. Empirically, we find that this requirement is satisfied for $t_{\mathrm{eff}} = 4.5/E_0$ for all ensembles used in this work. This approach provides a strict lower bound on the correlation function that is not affected by local fluctuations.

Via eq. (2.17), the bounds on the energy E_0 and E^*_{eff} are translated into bounds on the correlation function. By replacing the measured correlation function with its upper and lower bounds for $t > t_c$ in eq. (2.7), we obtain corresponding constraints on $a_\mu^{k,l}$ that depend on t_c. At the value of t_c where the central values of both bounds are compatible within the $1\,\sigma$ uncertainty of their respective counterpart, we average over the mean of the two bounds in a region of 0.25 fm or at least 4 time slices, to smooth out local fluctuations.

On ensembles with periodic boundary conditions in the temporal direction, we extend the above boundaries to include the contributions of wrappers around the temporal direction of the torus, which are small in all cases that are considered. For the ensembles A653, A654 and B450 with $m_\pi > 335\,\mathrm{MeV}$ and small temporal extents, we perform a fit to a single-state in the region around $T/2$ and replace the correlator at large times by the corresponding single-exponential form [51]. Note that this treatment is only possible due to the large pion mass on these ensembles such that a single stable state dominates.

For two ensembles, D200 at $m_\pi \approx 200\,\mathrm{MeV}$ and E250 at $m_\pi \approx 130\,\mathrm{MeV}$, we increase the statistical precision in the long-distance tail further by supplementing the LMA calculation with an explicit reconstruction of the isovector correlation function in terms of two-pion

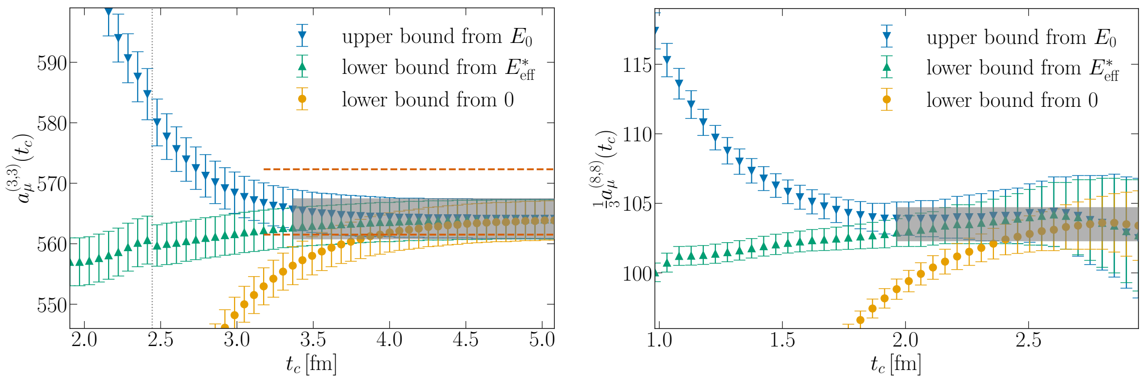

Figure 1. Determination of $a_\mu^{k,l}$ using the bounding method. t_c denotes the time where the correlator is replaced by the single state exponential as detailed in eq. (2.17). The downward triangles show the upper bound from the estimate of the ground state energy. The lower bound from the effective mass is given by the upward triangles, and the lower bound from setting the correlator to zero beyond t_c, which is just shown for comparison, is represented by the circles. The gray area indicates the final estimate. *Left:* In the isovector channel on ensemble E250. The dotted vertical line denote the switching point between the LMA and the spectroscopy correlation functions. The dashed horizontal lines indicate the starting time and the $1\,\sigma$ uncertainty band of the estimate that would be obtained when using only the LMA data set. *Right:* In the isoscalar channel on ensemble J303.

states, similarly to what was done in [34]. To this end, we have computed the lowest-lying energies E_n and corresponding amplitudes Z_n for the vector-vector, as well as the derivative of the vector-tensor currents, see [52–54]. Full details on the computation of the finite-volume energies and matrix elements at physical pion mass are deferred to appendix D.

For D200 and E250, we observe that the isovector correlation function is fully saturated by the three lowest states starting at $t \gtrsim 1.1\,\text{fm}$ and by the four lowest states starting at 1.5 fm, respectively. However, since LMA still yields smaller statistical errors for source-sink separations below about 2.5 fm, we only switch to the reconstructed isovector correlator when the latter is statistically more precise. In this way we are able to eliminate the exponential growth of the relative statistical noise, which is also encountered for LMA (albeit at a much reduced level), since the signal-to-noise ratio varies only slowly for the spectrally reconstructed correlator. We stress that the reconstruction in terms of the four lowest-lying states occurs in a region where all higher states have clearly decayed below any statistical significance.

We illustrate the bounding method for the isovector channel on the physical mass ensemble E250 and for the isoscalar channel on the finer lattice spacing ensemble J303, as shown in figure 1. The blue triangles denote the upper bound on $a_\mu^{k,l}$ based on the estimated ground state energy, while the green upward triangles depict the lower bound from the effective mass. For comparison, we also display a less strict lower bound obtained by setting $G^{(k,l)}$ to zero for $t > t_c$. The gray area represents the estimate for $a_\mu^{k,l}$, bounded by the two limits, and begins at the time separation where we start averaging the two.

In the left hand panel, the dotted vertical line indicates the time separation where we switch from the LMA to the reconstructed correlation function.[1] The dashed vertical lines show the uncertainty range of the estimate that would be obtained from using only the LMA correlation function.

2.5 Physical point extrapolation

Our strategy to approach the physical point consists in a combined chiral-continuum extrapolation of our lattice data. Whereas the continuum limit is mostly constrained by ensembles that feature larger-than-physical pion masses, precise data at near-physical values of the quark masses ensure that the interpolation in m_π^2 is well controlled. To disentangle strange from light quark mass effects, we have added four ensembles with physical strange quark mass to our standard set of ensembles, for which the sum of the bare quark masses is held constant along a chiral trajectory.

As outlined in [34], see also [55], a strong chiral dependence with a leading term proportional to $1/m_\pi^2$ or $\log(m_\pi^2)$ can be expected in the long-distance regime of a_μ^{hvp}. Our set of ensembles (see section 2.2) allows us to constrain the pion mass dependence of the observables that are studied in this work in the full range $m_\pi \in [131, 430]\,\mathrm{MeV}$. We point out that the region below 220 MeV is especially finely sampled and that three ensembles with approximately physical values of the quark masses enter the interpolation, with the data set on ensemble E250 being one of the statistically most precise ones.

For the Wilson quark action used in this work, distortions of the pion spectrum that could affect the long-distance tail are absent, in contrast to staggered or Wilson twisted-mass discretizations. Data computed for six values of the lattice spacing allow us to resolve leading and subleading cutoff effects. At our level of precision, we have to reckon with the occurrence of non-negligible mass-dependent cutoff effects. These can be reliably constrained since we cover the full range of pion masses on four of the six values of the lattice spacing that enter our result. In a future update, a significant increase in the number of available configurations for ensemble F300 will play a crucial role for further reducing the systematic uncertainty of the continuum extrapolation at the physical pion mass.

The small-a behaviour of a (lattice) regularized quantum field theory is described by Symanzik effective theory, which is expected to work well for the observable $(a_\mu^{\mathrm{hvp}})^{\mathrm{LD}}$. As pointed out in [56] for the case of QCD, the leading dependence on the cutoff is modified by logarithmic corrections and can be expressed as $a^{n_{\min}}\,[\alpha_{\mathrm{s}}(1/a)]^{\hat{\Gamma}}$, where $\hat{\Gamma}$ is the leading anomalous dimension. The Wilson quark action and the currents used in our work are non-perturbatively $\mathrm{O}(a)$-improved such that $n_{\min} = 2$. As explained in ref. [57], for our choice of action the term with $\hat{\Gamma} = 0.76$ is expected to dominate the description of cutoff effects in spectral quantities and those from the sea, while $\hat{\Gamma} = 0.395$ is the lowest non-zero anomalous dimension for quark bilinears with vector quantum numbers [58]. A potentially dangerous slowing down of the continuum extrapolation due to large negative anomalous dimensions can thus be excluded thanks to the existing analytic knowledge for our action. While it is not possible to resolve one or more anomalous dimensions in the existing range

[1]Note that the bounding method does not have to be applied as soon as the reconstructed correlation function is employed because the noise is under control in this case.

of lattice spacings, all of our continuum extrapolations include the possibility of a non-zero anomalous dimension for the leading term.

To convert the muon mass in the QED kernel function to lattice units and to form dimensionless quantities that act as proxies for the quark masses in our ensembles, we use the pion decay constant af_π. This approach, known as f_π-rescaling, was introduced in [34]. The key benefit of this strategy is the mitigation of the quark mass dependence in the isovector contribution to $(a_\mu^{\rm hvp})^{\rm LD}$ via a partial cancellation from the corresponding dependence of the decay constant. For each of our ensembles, we calculate af_π as outlined in appendix E of [18] and apply corrections for the leading finite-size effects, following [59]. The renormalization and improvement procedure utilizes the results for $Z_{\rm A}$ from [60] and $b_{\rm A}$, $\bar{b}_{\rm A}$ from [61]. To reduce fluctuations in the decay constants, we perform a fit to the values obtained from all large-volume ensembles. This fit is guided by the expectations from SU(3) chiral perturbation theory [62]. The fitted results are then evaluated for the parameter values specific to each ensemble, ensuring a stable and consistent representation of the decay constants.

The fit proceeds by forming a dimensionless combination of the decay constant and the flow quantity $\sqrt{t_0}$. The physical value of $\sqrt{t_0}$ is irrelevant for this purpose since we perform a local interpolation of the data. The quark mass dependence of the pion decay constant is then parameterized using the two variables

$$y = \frac{m_\pi^2}{8\pi^2 f_\pi^2} \propto m_{\rm l}\,, \qquad y_{K\pi} = \frac{m_K^2 + \frac{1}{2}m_\pi^2}{8\pi^2 f_{K\pi}^2} \propto 2m_{\rm l} + m_{\rm s}\,, \tag{2.18}$$

where $f_{K\pi} = \frac{2}{3}(f_K + \frac{1}{2}f_\pi)$. The specific physical values that define our hadronic scheme are collected in appendix A. It is worth noting that only a small deviation from the physical value of $y_{K\pi}$ is observed among the ensembles used in this work.

We refer to the pion decay constant at finite lattice spacing and physical values of y and $y_{K\pi}$ as $a\tilde{f}_\pi$. It is obtained according to

$$a\tilde{f}_\pi = \left(\frac{a}{\sqrt{t_0^{\rm sym}}}\right) \cdot \left(\frac{\sqrt{t_0^{\rm sym}}}{\sqrt{t_0^{\rm phys}}}\right) \cdot \left(\sqrt{t_0} f_\pi\right)_{\rm phys}\,, \tag{2.19}$$

with the first two factors taken from [37], the second being evaluated in the continuum. The quantity $\left(\sqrt{t_0} f_\pi\right)_{\rm phys}$ is obtained from the fit described above at physical values of y and $y_{K\pi}$ for each value of the lattice spacing.

For our fits to the various contributions to $(a_\mu^{\rm hvp})^{\rm LD}$ we proceed as follows. The proxies for the light quark mass and the sum of the sea quark masses are defined by

$$y = \frac{m_\pi^2}{8\pi^2 f_\pi^2} \propto m_{\rm l}\,, \qquad z = \frac{m_K^2 + \frac{1}{2}m_\pi^2}{8\pi^2 \tilde{f}_\pi^2} \propto 2m_{\rm l} + m_{\rm s}\,. \tag{2.20}$$

Compared to $y_{K\pi}$, we find that the simpler quark mass dependence of z helps us to disentangle the two directions in the quark mass plane and to separate cutoff effects. The quantity $a/\sqrt{t_0}$ serves as a proxy for the lattice spacing. For the muon mass entering the QED kernel used on a given ensemble, we use $am_\mu = (af_\pi) \cdot (m_\mu/f_\pi)^{\rm phys}$ for the isovector contribution, with af_π computed on that ensemble, while $am_\mu = (a\tilde{f}_\pi) \cdot (m_\mu/f_\pi)^{\rm phys}$ is used for the other contributions. This strategy prevents the chiral dependence of the pion decay constant from affecting the isoscalar contribution while ensuring a consistent scale setting across all our observables. We summarize the values of the bare lattice quantities and quark mass proxies in table 6.

We follow the general strategy of our previous works [18, 22] to extrapolate to the physical point by performing a simultaneous fit of our data to the quark mass and cutoff dependence. Denoting the light quark mass proxy by $X_\pi \propto m_{\rm l}$, we describe the continuum light quark mass dependence with the general ansatz

$$\begin{aligned}\mathcal{O}(X_\pi) = \mathcal{O}(X_\pi^{\rm phys}) &+ \gamma_1 \left(X_\pi - X_\pi^{\rm phys}\right) \\ &+ \gamma_2 \left(f_{\rm ch,1}(X_\pi) - f_{\rm ch,1}(X_\pi^{\rm phys})\right) \\ &+ \gamma_3 \left(f_{\rm ch,2}(X_\pi) - f_{\rm ch,2}(X_\pi^{\rm phys})\right) \\ \text{where } f_{\rm ch,1} &\in \{1/X_\pi\,;\ \log(X_\pi)\,;\ X_\pi \log(X_\pi)\,;\ X_\pi^2\}\,, \\ \text{and } f_{\rm ch,2} &\in \{1/X_\pi\,;\ X_\pi^2\}\,.\end{aligned} \tag{2.21}$$

Here we always include the leading term $\propto X_\pi$ and test for the significance of the higher order terms on a case-by-case basis. The dependence on the quark mass proxy $X_{\rm K} \propto 2m_{\rm l} + m_{\rm s}$ is always parameterized via

$$\mathcal{O}(X_{\rm K}) = \mathcal{O}(X_{\rm K}^{\rm phys}) + \gamma_0 \left(X_{\rm K} - X_{\rm K}^{\rm phys}\right)\,. \tag{2.22}$$

and allows us to correct for small deviations from $X_{\rm K}^{\rm phys}$.

Denoting the proxy for the lattice spacing with $X_a \propto a$, our most general ansatz for the dependence on the lattice spacing in this work is

$$\mathcal{O}(X_a) = \beta_2 \left[\alpha_{\rm s}(1/X_a)\right]^{\hat\Gamma} X_a^2 + \beta_3\, X_a^3 + \delta_2 \left[\alpha_{\rm s}(1/X_a)\right]^{\hat\Gamma} X_a^2 \left(X_\pi - X_\pi^{\rm phys}\right)\,, \tag{2.23}$$

where $\hat\Gamma \in \{0, 0.395\}$. We always include the leading term with the coefficient β_2 and test for higher order cutoff effects as well as quark mass dependent cutoff effects by including/excluding the terms proportional to β_3 and δ_2. We perform every fit for each of the two choices for the anomalous dimension $\hat\Gamma$ that have been motivated above. We use the five-loop running relation from [63], using as input $\Lambda_{\overline{\rm MS}}^{(3)}$ [64], to evaluate the running-coupling constant at the scale $1/a$.

Further variations are introduced by applying cuts to the data that enter the fits. In addition to fitting the whole data set, we also consider fits in which the coarsest or the two coarsest values of the lattice spacing are excluded. To avoid overfitting when removing data from the two coarsest lattice spacings, we do not include terms that parameterize higher-order cutoff effects. We also perform fits that exclude ensembles with pion masses larger than 400 MeV, thereby removing data at the SU(3)-symmetric point. Further cuts in the pion mass are not considered because this would exclude both of our ensembles at the finest lattice spacing of $a \approx 0.039$ fm.

To quantify the systematic uncertainty from the extrapolation to the physical point and to determine our final results, we perform a model average over the different fit forms that are considered in this work. As done in our previous works and following ref. [65], we use the Akaike Information Criterion (AIC) [66] to assign a weight to each fit. The central value and its statistical uncertainty are then obtained from a weighted average over all analyses, whereas the systematic uncertainty is obtained from the distribution of weighted models. We test explicitly that using the information criterion that has been defined in [14] leads to negligible differences in our final results. The determination and propagation of statistical uncertainties is performed using the Γ-method in the implementation of the `pyerrors` package [67–69]. Significant autocorrelations are present at small lattice spacing, and we reliably take them into account for all observables considered in this work.

2.6 Finite-volume correction

Finite-volume effects are sizeable in the long-distance regime of the isovector correlation function. The origin of these effects lies in the discrete nature of the low-lying multi-pion spectrum when the theory is formulated in finite volume. Accordingly, it is mandatory to apply a correction for finite-size effects lest the latter become dominant in the final error budget.

As in our previous works [18, 35], we employ two methods to correct our data for finite-size effects. Based on the electromagnetic form factor of the pion in the spacelike region, the method by Hansen and Patella (HP) [70, 71] is expected to work especially well in the short and intermediate distance regions. The Meyer-Lellouch-Lüscher (MLL) formalism is based on the timelike pion form factor [72] and expected to be most successful in the long-distance region, where only a few states contribute significantly in the spectral decomposition of the correlation function.

We follow our strategy from [18] and apply the Hansen-Patella method to correct the isovector correlation function for source sink separations below $t^* = (m_\pi L/4)^2/m_\pi$. From then on, we employ the MLL formalism. Accordingly, the latter dominates the correction for $(a_\mu^{\mathrm{hvp}})^{\mathrm{LD}}$ close to the physical value of the pion mass.

Motivated by its phenomenological success and simplicity, we use the vector-meson-dominance (VMD) parameterization of the pion form factor in the HP volume correction, $F_\pi(-Q^2) = M_{\mathrm{VMD}}^2/(Q^2 + M_{\mathrm{VMD}}^2)$, while the Gounaris-Sakurai (GS) parameterization is used in the MLL method. In order to make the form factor consistent on the space- and time-like sides, we proceed by matching the value of the VMD form factor with the GS one at virtuality $Q^2 = M_\rho^2$, where M_ρ is the ρ meson mass entering the GS parameterization. The VMD and GS parameterizations then agree to within one percent for all virtualities $0 \leq Q^2 \leq 0.8\,\mathrm{GeV}^2$. As a result, when comparing the corrections that are predicted by the HP and MLL formalisms with each other, we find that they are consistent at the level of 5% and that any discontinuity in the finite-size correction on $G^{(3,3)}(t)$ at the time $t = t^*$ is a very small effect in comparison to the correction itself.

As in [18, 35], we also correct for the effect from kaons propagating in the finite box, which is relevant for ensembles close to the SU(3) symmetric point on the chiral trajectory where $\mathrm{Tr}[M_{\mathrm{q}}] = \mathrm{const}$. We use the HP formalism to compute the corresponding correction.

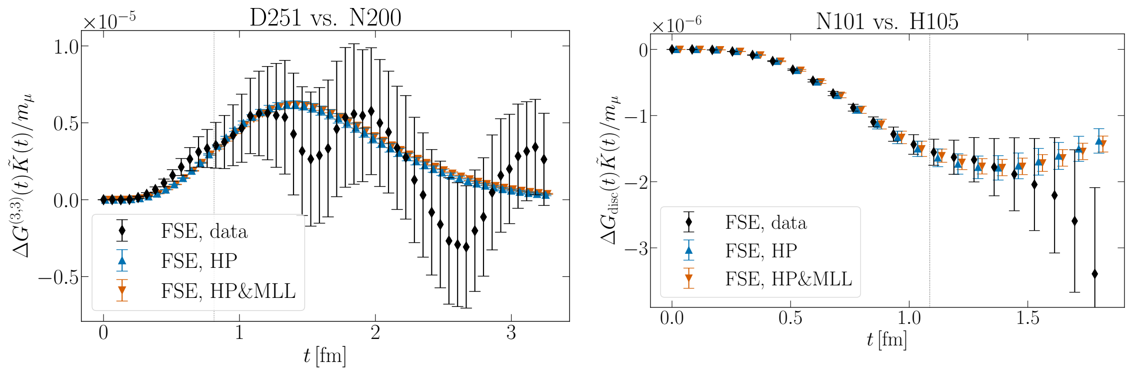

Figure 2. Illustration of finite-volume effects on the integrand for the light-connected and disconnected contributions. Black diamonds denote effects computed from lattice QCD in two volumes. Blue upward triangles show corrections predicted by the HP method, while red downward triangles represent corrections using the MLL method beyond $t^{\star}$, indicated by the vertical dotted line for the respective smaller volume. *Left:* Light-connected contribution for ensembles D251 and N200. *Right:* Disconnected contribution for ensembles N101 and H105.

While we previously corrected the data for the entire finite-size effect before performing the chiral-continuum extrapolation, we now follow a different procedure set out in [14]. We first apply the finite-volume correction on all ensembles to match a common reference value of $m_\pi L$ and then extrapolate the results to the physical point. By choosing a reference value of $m_\pi L$ close to the one corresponding to our physical pion mass ensembles, we minimize the correction that is applied to our most important data. Furthermore, to facilitate the comparison with the results of [14] without the need for a finite-volume correction with the associated uncertainty, we define our reference target to be

$$(m_\pi L)^{\mathrm{ref}} = (m_{\pi^0})_{\mathrm{phys}} \cdot 6.272\,\mathrm{fm} \approx 4.290\,. \tag{2.24}$$

The correction from this reference value to the infinite-volume limit is performed in the continuum.

We find an excellent agreement of the HP&MLL method with the effects that we see in our data. This is illustrated in figure 2, where we show in black the differences between the integrands for the isovector contribution for a_μ^{hvp} as computed on the ensembles D251 and N200 with $m_\pi \approx 286\,\mathrm{MeV}$. Both ensembles differ only in their spatial extent and feature $(m_\pi L)^{\mathrm{D251}} = 5.9$ and $(m_\pi L)^{\mathrm{N200}} = 4.4$. The statistical uncertainty of this difference is mainly driven by the smaller box N200. Together with the finite-volume effect from the data, we show the corresponding finite-volume correction as predicted by our models. The blue data set denotes the correction as given by HP, whereas the orange data uses HP up to t^* and MLL from then on. Both methods agree very well with each other and also – as far as can be judged given the statistical uncertainties – with the lattice data.

On the right hand side of figure 2 we show a similar comparison for the disconnected contribution in the (u, d, s) quark sector on the ensembles N101 and H105 at a similar pion mass but coarser lattice spacing, corresponding to the effect from $(m_\pi L)^{\mathrm{H105}} = 3.9$ to $(m_\pi L)^{\mathrm{N101}} = 5.8$. We use the same models, with the appropriate prefactor $-\frac{1}{9}$ [73, 74], to predict the difference. Again, an excellent agreement between the prediction and the data for the finite-size correction can be observed in the region where the statistical uncertainties of the data are still small. We note that, while this test further increases our confidence in the correction, it will not be applied in our analysis since we work with the isoscalar contribution, where the leading finite-volume effects of light-connected and disconnected contributions cancel. As we only correct for finite-size effects from the isovector, the agreement between the prediction in the right panel of figure 2 and the lattice data is evidence for the smallness of these effects in the isoscalar channel.

For the final conversion of our continuum results at physical quark masses from the reference volume specified in eq. (2.24) to infinite volume, we use the HP correction up to t^* and MLL from then on. The GS parameters for the pion form factor are taken from the dedicated calculation on ensemble E250 described in appendix D and a forthcoming publication [75]. The VMD mass entering the HP method is based on the pion charge radius $r_\pi = 0.659(4)\,\mathrm{fm}$ from [76] and we do not find any significant deviation if we instead match to the GS form factor as described above.

The correction applied is

$$(a_\mu^{\mathrm{hvp}})^{\mathrm{LD}}(L=\infty) - (a_\mu^{\mathrm{hvp}})^{\mathrm{LD}}(L_{\mathrm{ref}}) = 16.7(1.5)\,. \tag{2.25}$$

The absolute uncertainty we have assigned to it is mainly based on the sensitivity of the correction to the values of the GS parameters as well as to the difference to the next-to-next-to-leading order chiral perturbation theory expression given in [77], which we find to be on the order of 0.2. We have also estimated the finite-size effect associated with higher channels. Specifically, we have studied the $\pi^+\pi^-\pi^0\pi^0$ channel, approximating it as an $\omega\pi$ channel. From here, using the cross-section measurement [78], we have estimated the finite-size effect in the approximation that there are discrete, non-interacting $\omega\pi^0$ energy levels on the torus, finding an absolute effect on a_μ^{hvp} in the range 0.2 to 0.3.

In addition to the finite-size effects affecting the isovector channel, we have also considered those affecting the isoscalar channel. One expects, on one hand, a contribution from $\bar{K}K$ states, which we take into account via the HP formalism. These effects are of order $\exp(-m_K L)$. There are however also finite-size effects of order $\exp(-m_\pi L)$, associated mainly with the three-pion channel. As pointed out in [14], these are heavily suppressed in the chiral power-counting compared to the isovector channel; indeed it takes three pions and three derivatives to form an isoscalar current, $\epsilon_{\mu\nu\alpha\beta}\partial_\nu\pi^+\partial_\alpha\pi^-\partial_\beta\pi^0$ [79, 80]. We expect the numerically leading effect to come from a slight shift of the finite-volume energy level associated with the ω meson, and possibly with the higher-lying three-pion states. In the former case, a lattice study [81] of energy levels in the isoscalar channel has recently appeared for a pion mass of 200 or 300 MeV; no statistically significant shift of the lowest-lying level was found between $L = 2.5\,\mathrm{fm}$ and $L = 3.7\,\mathrm{fm}$. In the case of the three-pion states above one GeV, we approximate them as being mainly in a $\rho\pi$ configuration and estimate the associated finite-size effect in the same way as in the $\omega\pi$ case described in the previous paragraph; however, the corresponding $e^+e^- \to \pi^+\pi^-\pi^0$ cross-section is a factor of about three smaller at those energies than $e^+e^- \to \pi^+\pi^-\pi^0\pi^0$, further reducing the importance of this effect. Based on the above discussion, we do not include any finite-size correction for the isoscalar channel, but assign an absolute uncertainty of 0.3 to this effect.

3 Results

In this section, we describe our calculation of $(a_\mu^{\mathrm{hvp}})^{\mathrm{LD}}$ in isospin-symmetric QCD. Combining the result with our earlier determinations of $(a_\mu^{\mathrm{hvp}})^{\mathrm{SD}}$ [22] and $(a_\mu^{\mathrm{hvp}})^{\mathrm{ID}}$ [18] allows us to present an updated result for a_μ^{hvp} with respect to [34]. As in our earlier work, we prefer to perform an isospin decomposition of the electromagnetic current and first present the computation of the isovector and isoscalar contributions to $(a_\mu^{\mathrm{hvp}})^{\mathrm{LD}}$. To facilitate the comparison with other groups, we also provide results for individual flavour components. Based on an estimate for the leading isospin-breaking effects, we compute an updated value of a_μ^{hvp} that can be directly compared to experiment.

3.1 The isovector contribution

The isovector contribution dominates by far the central value and the uncertainty of a_μ^{hvp} and $(a_\mu^{\mathrm{hvp}})^{\mathrm{LD}}$. Therefore, its precise computation is the main focus of this work. As explained in section 2.4, we use a combination of noise reduction methods to compute the isovector correlation function to high accuracy, especially at close-to-physical pion masses where the signal-to-noise problem is enhanced.

Here, we focus specifically on the combination of noise reduction techniques applied on ensemble E250 at (slightly smaller than) physical value of the pion mass. Whereas stochastic sources have been utilized to determine the isovector correlation function on this ensemble in [34], we now employ LMA to maximize the extractable information in the long-distance tail from the gauge ensemble. The computation is described in detail in appendix C, and the expected dominance of low modes in the tail is highlighted in figure 12. When used in combination with the bounding method, we find that LMA alone allows us to reduce the uncertainty on a_μ^{hvp} from 2.2% in ref. [34] to 0.8% in this work. In figure 3 we show the integrand to compute $(a_\mu^{3,3})^{\mathrm{LD}}$ on E250, where the black diamonds denote the integrand computed from the LMA correlation function.

Recalling that the isovector correlator in the long-distance regime is dominated by two pions, we have also performed a dedicated study to determine the spectrum of the lowest-lying two-pion states and their overlap with the isovector current (see appendix D for an in-depth description). The coloured data points in figure 3 show the accumulated contributions of an increasing number of two-pion states to the TMR integrand. We find that four states saturate the correlator at a source-sink separation of about 1.5 fm. We note in passing that the largest energy level that enters this reconstruction is slightly above the mass of the ρ meson. As stated already in section 2.4, the correlation function that has been computed using LMA is more precise at this distance. However, since the signal-to-noise ratio deteriorates exponentially in the LMA correlation function whereas it stays basically constant for the correlator reconstructed from two-pion states, it is clear that there exists a distance above which the reconstruction is more precise. For our specific calculation, this happens for $t \gtrsim 2.4\,\mathrm{fm}$.

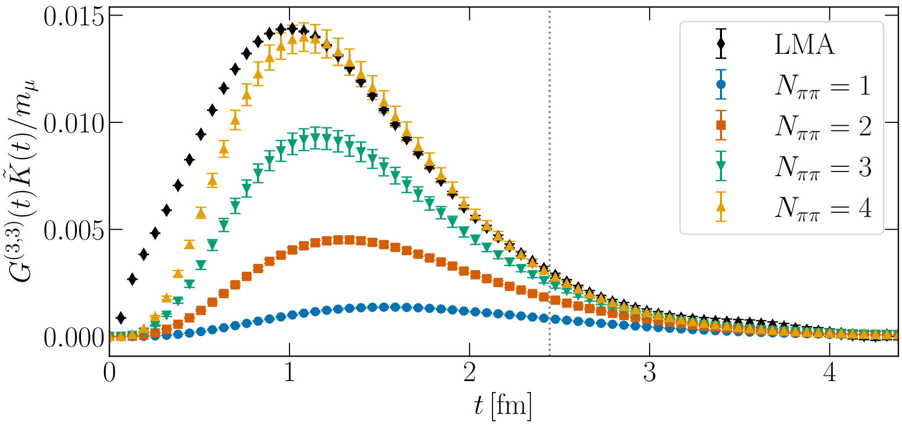

Figure 3. The integrand to compute $a_\mu^{3,3}$ on the physical mass ensemble E250. The black diamonds are based on the correlation function that is computed using LMA. The coloured data show the reconstructed integrand from $N_{\pi\pi}$ states. The vertical dotted line denotes the distance where we change from the LMA to the spectroscopy data set.

To combine the two sets of data, we follow one of the methods that have been explored in our previous work [34] and replace the directly computed correlation function with the reconstructed one beyond a specific source-sink separation where the reconstructed correlation function is more precise. We note that neglected contributions from higher states are even less significant for these larger source-sink separations. Four-pion states have been shown to be numerically irrelevant in [82], since their overlap with the isovector correlator is very small. The combination of the two data sets allows us to further reduce the relative uncertainty of $a_\mu^{3,3}$ on this ensemble by a factor of two to 0.4% (excluding the uncertainty of the scale setting quantity). Since ensemble E250 has close-to-physical quark masses, this result provides a strong constraint for the chiral-continuum fit and has a direct influence on the attainable precision at the physical point. The second ensemble where we employ spectroscopy data is D200 with $m_\pi \approx 200\,\text{MeV}$. With respect to the previous application in [34], we have added an LMA computation of the isovector correlation function. The combination of both methods reduces the statistical uncertainty by about 25% on this ensemble, compared to pure LMA.

Across our set of 34 gauge ensembles, we reach a precision of 0.35%$-$1.5% for $a_\mu^{3,3}$ and 0.55%$-$2.4% for $(a_\mu^{3,3})^{\text{LD}}$ (see table 7 for an overview of results). We find that high-precision results on ensembles with close-to-physical pion masses are crucial to constrain our global fit in the relevant region of the parameter space. For most of the ensembles with lattice spacings $a \leq 0.05\,\text{fm}$, autocorrelations limit the attainable precision such that longer Monte Carlo chains are needed to reduce the uncertainties.

As outlined in section 2.5, we scan over a variety of fit forms and data selections to determine our final result at the physical point from a model average. For the chiral dependence, see eq. (2.21), we find that fits without a chirally divergent term do not lead to acceptable fit quality, which is why we exclude them from the model average. The term $1/X_\pi$ in $f_{\text{ch},2}$ is only used in conjunction with $\log(X_\pi)$ in $f_{\text{ch},1}$, following an observation in

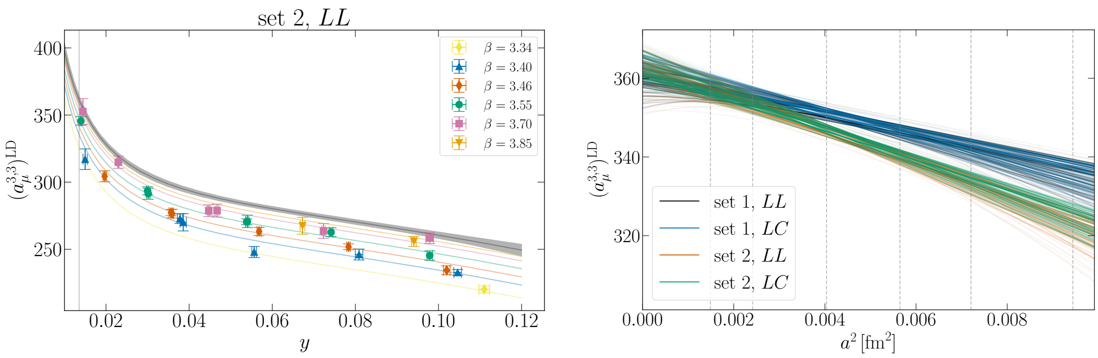

Figure 4. Chiral-continuum extrapolation of the isovector contribution to $(a_\mu^{\mathrm{hvp}})^{\mathrm{LD}}$. *Left:* Illustration of the best fit according to the AIC to the data based on the improvement scheme set 2 and the LL discretisation. The data points denote the result for each ensemble, corrected for a deviation from the physical value of z. The black line denotes the chiral dependence in the continuum limit and the grey area the statistical uncertainty. The coloured lines correspond to the chiral dependence at non-zero lattice spacing. *Right:* Approaches to the continuum limit for four sets of data based on the improvement schemes of set 1 and 2 and the LL and LC discretizations of the current based on a scan over fit models. Each line shows the result from one single fit and the opacity of the lines corresponds to the weight of the fit in the model average. Dashed vertical lines indicate the lattice spacings used in this work. The conversion to fm has been performed for illustrative purposes only.

[55] that this combination could be favoured for pion masses below the physical point. This leads to five different ansätze for the chiral behaviour that are combined with eight ansätze for the continuum extrapolations and four subsets of the data.

Upon inspecting the different classes of fits with their respective model weights, we make the following observations. Fits that only include a single term to parameterize the lattice spacing dependence generally have good quality and are thus preferred over fits that include higher-order lattice artifacts, which however have a non-negligible model weight. Fits that include mass-dependent cutoff effects favour slightly larger values of $(a_\mu^{3,3})^{\mathrm{LD}}$ at the physical point than fits without this extra term. Varying the anomalous dimension $\hat{\Gamma}$ does not lead to significant changes in the fit quality or the result in the continuum limit. However, fits with a non-zero anomalous dimension prefer slightly smaller values of $(a_\mu^{3,3})^{\mathrm{LD}}$.

The chiral behaviour is tightly constrained by the precise data point of the E250 ensemble at physical pion mass. Two parameters are sufficient to describe the chiral behaviour with good fit quality. The inclusion of a third parameter to parameterize the dependence on the squared pion mass leads to an insignificant shift towards larger values of $(a_\mu^{3,3})^{\mathrm{ID}}$.

The left-hand side of figure 4 depicts the chiral-continuum extrapolation with the highest model weight for the LL discretization of the vector current, using set 2 of the improvement and renormalization coefficients. No cuts in the data have been applied in this instance. The data are adjusted for deviations from z^{phys} and presented alongside the evaluation of the chiral behaviour at finite lattice spacing (shown by the coloured lines) and in the continuum limit (represented by the grey error band). As can be seen from the figure, the chiral dependence is well constrained over the full range of pion masses. This includes the region $m_\pi < 230\,\mathrm{MeV}$ or $y < 0.04$, respectively, which is sampled by eleven gauge ensembles and exhibits a strong curvature.

The panel on the right-hand side of figure 4 illustrates the continuum extrapolation at physical quark masses for each of the fits included in the model average across four data sets. Each fit is represented by a line whose opacity corresponds to the weight in the model average for the respective data set. The local and conserved discretizations of the vector current show only marginal differences. Comparing sets 1 and 2, a small difference is observed at finite lattice spacing, which, as anticipated, disappears in the continuum limit where all extrapolations are in close agreement.

For the coarsest lattice spacing, the relative size of the cutoff effects is about 10%, while the extrapolation from the finest lattice spacing is very small. We note that replacing the scale setting quantity by, for instance, $\sqrt{t_0}$ or w_0, has a significant impact on the magnitude of the cutoff effects. From this observation, we infer that the relative cutoff effects between $(a_\mu^{\mathrm{hvp}})^{\mathrm{LD}}$ and the scale setting quantity dominate over the intrinsic cutoff effects of $(a_\mu^{\mathrm{hvp}})^{\mathrm{LD}}$ itself. More precise data points at the two finest lattice spacings will help to further constrain the continuum extrapolation.

Our final result in the reference volume, based on the LL discretization and set 2 is

$$(a_\mu^{3,3})^{\mathrm{LD}}(L_{\mathrm{ref}}) = 362.0(3.7)_{\mathrm{stat}}(2.7)_{\mathrm{syst}}[4.6]\,. \tag{3.1}$$

We note that statistical uncertainties dominate over the systematic uncertainties from the variation of the fit models. The final uncertainty of the long-distance, isovector contribution in finite volume, reported in square brackets and obtained by adding statistical and systematic uncertainties in quadrature, is at the level of 1.3%. Combining the result of eq. (3.1) with the finite-volume effects that have been computed in eq. (2.25) for the isovector channel, we obtain

$$(a_\mu^{3,3})^{\mathrm{LD}} = 378.7(3.7)_{\mathrm{stat}}(3.1)_{\mathrm{syst}}[4.8]\,. \tag{3.2}$$

3.2 The isoscalar contribution

At the SU(3) symmetric point, where light and strange quark masses are equal, the quark-disconnected contribution from light and strange quarks vanishes, and the isoscalar contribution is trivially related to the isovector one. As one approaches the physical values of quark masses, a strong signal-to-noise problem is observed, since the absolute error of the quark-disconnected correlation function remains constant as a function of the source-sink separation. As described in section 2.4, we employ the bounding method to obtain reliable estimates for $(a_\mu^{8,8})^{\mathrm{LD}}$.

In contrast to the isovector case, where some of our most precise data points are at small pion masses, we find that statistical uncertainties in the isoscalar channel grow towards physical quark masses. However, the chiral dependence in the isoscalar channel is much more benign, as the singular behaviour of light-connected and disconnected contributions in the isoscalar channel cancels, as do the leading finite-size effects. We perform a small finite-size correction of the strange-connected contribution, which is relevant only at or near

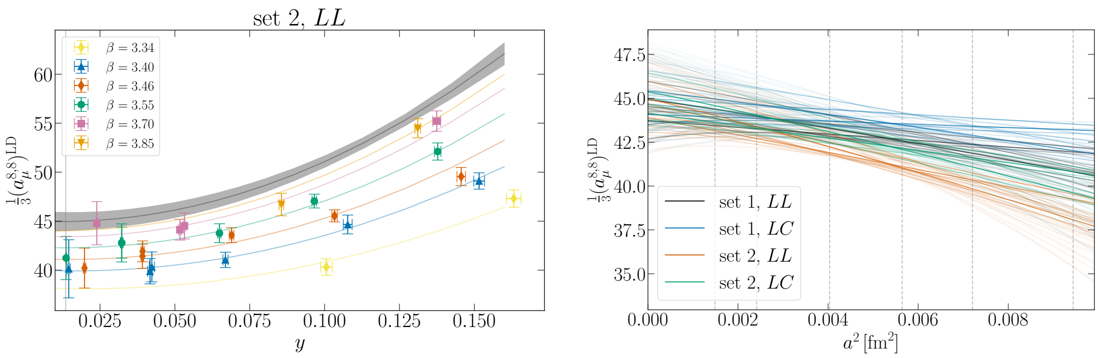

Figure 5. Same as figure 5 for the isoscalar contribution.

the SU(3)-symmetric point, where the kaon mass is relatively small ($m_K L \geq 5.1$ across all of the ensembles entering the final fits).

To describe the chiral dependence of the isoscalar contribution, we only include terms that do not diverge in the chiral limit and find the variation of the results for different ansätze to be mild. Fits that include mass-dependent cutoff effects are strongly favoured by the AIC and lead to smaller results at the physical point, compared to fits with pure a^2 cutoff effects. Models with non-zero anomalous dimension have very similar fit quality compared to fits with $\hat{\Gamma} = 0$ and lead to slightly larger results in the continuum limit.

The left-hand side of figure 5 shows our best fit for set 2 and the LL discretization, which employs two terms to describe the chiral dependence of the data. The dependence on the variable z (see eq. (2.20)), which is expected due to the strange-quark mass content of the isoscalar contribution, is well described by the linear term in our fit ansatz and constrained by the four ensembles on the chiral trajectory where the strange quark mass is kept near its physical value.

The scan over the different ansätze to perform the continuum extrapolation is depicted on the right hand side. Again, the variation between the different discretization prescriptions is negligible in the continuum. Based on the model average, we find

$$\frac{1}{3}(a_\mu^{8,8})^{\mathrm{LD}} = 44.5(1.2)_{\mathrm{stat}}(1.1)_{\mathrm{syst}}(0.3)_{\mathrm{FV}}[1.6]\,, \tag{3.3}$$

for the isoscalar contribution, including the numerically irrelevant estimate of 0(0.3) for the finite-volume correction, see section 2.6. Statistical and systematic uncertainties have a similar size and the combined uncertainty is at the level of 3.6%, mainly driven by the statistical noise encountered for the quark-disconnected contribution.

3.3 Further contributions

The charm-connected contribution at long distances is very small since the correlator falls off quickly and, as described below, we find that its contribution to the total $(a_\mu^{\mathrm{hvp}})^{\mathrm{LD}}$ is smaller than the overall error. For our evaluation of the long-distance contribution, we employ the same data set as the one that has been used in [18, 22]. The charm quark is partially quenched in the sea of light and strange quarks, and we tune the hopping parameter to reproduce the D_s meson mass at finite lattice spacing (see appendix A). Statistical noise is irrelevant and we simply sum the integrand in the long-distance region. In line with [18, 22] we use the LC correlation function to compute the final result since it exhibits more benign cutoff effects. Our result

$$(a_\mu^{c,c})^{\mathrm{LD}} = 0.01409(35)_{\mathrm{stat}}(60)_{\mathrm{syst}}[69]\,, \tag{3.4}$$

is negligibly small with respect to the full $(a_\mu^{\mathrm{hvp}})^{\mathrm{LD}}$ and even the charm-connected contribution to a_μ^{hvp}, which arises predominantly from the short- and intermediate-distance windows.

Effects from charm-disconnected contributions have been shown to be numerically irrelevant already for the short-distance contribution in [22] such that we do not consider them here. We have estimated the effect from missing charm loops in our computation in appendix C of [18] and section H of [22] and expect them to be irrelevant in the long-distance regime compared with the uncertainties reported here. Note also that the RBC/UKQCD collaboration has investigated the effect of charm quenching on $(a_\mu^{\mathrm{hvp}})^{\mathrm{ID}}$ and did not find a numerically relevant contribution [21]. Furthermore, no evidence for a charm quenching effect on the quantity r_1 defined from the static potential is seen at the 1% level when comparing the results of [83] and [84] (the scale being defined by f_π in both cases; see the discussion in [85]). Dedicated studies of charm quenching effects on generic low-energy observables in [86, 87] find an effect at the level of 0.2%. We include this effect as additional uncertainty in our final estimate for $(a_\mu^{\mathrm{hvp}})^{\mathrm{LD}}$.

3.4 Flavour decomposition

To allow for cross-checks of the various contributions to $(a_\mu^{\mathrm{hvp}})^{\mathrm{LD}}$ among different lattice calculations, we also perform an analysis of the strange-connected contribution that enters our final result via the isoscalar contribution in eq. (3.3). After performing the model average, we find

$$\frac{1}{9}(a_\mu^{s,s})^{\mathrm{LD}} = 17.73(17)_{\mathrm{stat}}(13)_{\mathrm{syst}}[21]\,. \tag{3.5}$$

By combining this result with eq. (3.1), eq. (3.3) and eq. (2.25) we determine the disconnected contribution in the infinite-volume limit as

$$(a_\mu^{\mathrm{hvp}})^{\mathrm{LD}}_{\mathrm{disc}} = -15.3(1.2)_{\mathrm{stat}}(1.2)_{\mathrm{syst}}[1.6]\,. \tag{3.6}$$

To complete the set of results according to their decomposition in terms of quark flavours, we note that the light-quark connected contribution is obtained by multiplying the isovector contribution of eq. (3.2) by 10/9.

3.5 The long-distance contribution

We combine our results for isovector, isoscalar and charm-connected contributions in eqs. (3.2, 3.3, 3.4) in the infinite-volume limit to obtain

$$(a_\mu^{\mathrm{hvp}})^{\mathrm{LD}} = 423.2(4.2)_{\mathrm{stat}}(3.3)_{\mathrm{syst}}(0.8)_Q[5.4]\,, \tag{3.7}$$

	S				
O	f_π	f_K	m_π	m_K	m_{Ds}
$(a_\mu^{3,3})^{\mathrm{LD}}$	-1.8982	-0.0277	-0.5737	-0.2816	–
$(a_\mu^{8,8})^{\mathrm{LD}}$	-2.0891	$+0.1691$	$+0.0948$	-1.6577	–
$(a_\mu^{\mathrm{c,c}})^{\mathrm{LD}}$	$+0.6830$	$+1.6446$	-0.0695	$+0.0675$	-10.5355
$(a_\mu^{\mathrm{hvp}})^{\mathrm{LD}}$	-1.9190	-0.0061	-0.5005	-0.4322	-0.0004

Table 2. Dimensionless scheme dependencies of observable O with respect to the quantity S according to eq. (3.9).

for the long-distance contribution to a_μ^{hvp} in isospin-symmetric QCD, where we include an additional uncertainty due to the quenching of the charm quark, denoted by the subscript Q. Our hadronic scheme is defined by

$$\begin{aligned}
&f_\pi = 130.56\,\mathrm{MeV}, \qquad f_{\mathrm{K}} = 157.2\,\mathrm{MeV}, \\
&m_\pi = 134.9768\,\mathrm{MeV}, \quad m_K = 495.011\,\mathrm{MeV}, \quad m_{D_{\mathrm{s}}} = 1968.47\,\mathrm{MeV}\,.
\end{aligned} \tag{3.8}$$

More details can be found in appendix A. The conversion to other schemes can be easily performed using the information collected in table 2, where we list the dimensionless scale dependencies

$$\frac{S}{O}\frac{\partial O}{\partial S}\,, \tag{3.9}$$

for $O = (a_\mu^{3,3})^{\mathrm{LD}}$, $(a_\mu^{8,8})^{\mathrm{LD}}$, $(a_\mu^{\mathrm{c,c}})^{\mathrm{LD}}$, $(a_\mu^{\mathrm{hvp}})^{\mathrm{LD}}$ and each quantity S that is used to define the scheme. As anticipated, the dependence on f_{K} is strongly suppressed in the dominant contributions with respect to the dependence on f_π. For the numerically irrelevant charm-connected contribution, the scale dependence is dominated by the tuning of the valence charm quark mass. Small changes in the scheme can be performed a posteriori given the information provided in the table. To convert our results to a scheme that employs a different quantity to set the scale, such as the Ω baryon mass, the derivative of f_π and f_{K} with respect to this quantity must be determined.

Currently, there is only one other result [88] for the isovector contribution to $(a_\mu^{\mathrm{hvp}})^{\mathrm{LD}}$, while no further results currently exist for the isoscalar contribution. Before proceeding to comparisons, we comment on the dependence of the results on the chosen hadronic scheme that defines isoQCD. First, we remark that, on CLS ensembles, determinations of the flow-scale t_0 via the physical quantities $(f_K + \frac{1}{2}f_\pi)$ (1.0% precision, [36]), m_Ξ (0.6%, [37]), m_Ω (0.22%, [89]) and m_N (0.6%, [90]) yield consistent results within their respective uncertainties. Among the determinations by different collaborations of the flow scales t_0 and w_0 in terms of various input quantities (m_Ω, f_π, ...), however, somewhat more variation is observed. In particular, the determinations of t_0 from [84, 91] are significantly lower than that of [92], even though all three use $N_f = 2+1+1$ simulations and rely on f_π as input quantity. There is mild evidence that flow scales determined with Wilson-type

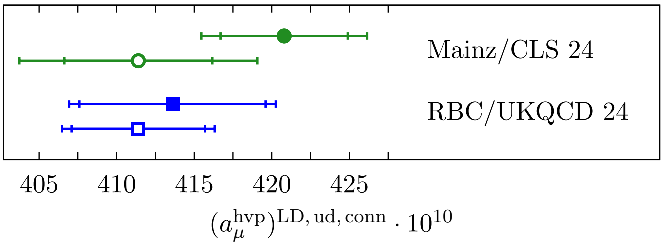

Figure 6. Overview of results for the light-connected contribution to $(a_\mu^{\mathrm{hvp}})^{\mathrm{LD}}$. Open symbols denote the results in the BMW20 scheme whereas results that are shown by filled symbols have been computed in the Mainz and RBC/UKQCD worlds, respectively.

fermions [36, 37, 92] are systematically larger than those obtained with staggered quarks, including the result in [14] for w_0 that defines the BMW20 scheme. At present, this makes it difficult to quantitatively address the question of the hadronic scheme dependence in the physical values of t_0 and w_0. However, the dependence of $(a_\mu^{\mathrm{hvp}})^{\mathrm{LD}}$ on the hadronic scheme could be relevant due to its high precision, its enhanced sensitivity to the scale setting and relatively large contributions from isospin-breaking corrections. The size of the latter is not yet precisely known, and care is needed when combining results from different isoQCD schemes.

In figure 6 we compare our results for $(a_\mu^{3,3})^{\mathrm{LD}}$ in our preferred scheme eq. (3.2) and in the BMW20 scheme eq. (A.7) with the recent determination by RBC/UKQCD [88] in their RBC/UKQCD18 scheme and in the BMW20 scheme [14]. We find excellent agreement between the two calculation when the same scheme is employed.[2] This is a reassuring indication of universality between two different lattice actions in the pure long-distance regime of a_μ^{hvp} and strengthens our confidence in the reliability of lattice QCD results for this quantity. However, the results differ noticeably when a different scheme is employed. While this is not unexpected in isospin-symmetric QCD, it is clear that any scheme dependence would have to be compensated upon properly including isospin-breaking effects.

We stress that we observe sizeable higher-order cutoff effect when w_0 is used to set the scale, leading to larger overall uncertainties in the continuum limit. This is why we have chosen f_π and f_{K} in $2+1$-flavour QCD as scale-setting quantities, as outlined in appendix A. By contrast, the BMW20 scheme is based on the Ω-baryon mass computed in $2+1+1$-flavour QCD+QED, which is used to determine the value of w_0 at the physical point. When the latter is used as input in our calculation in order to connect to the BMW20 scheme, we observe a shift in the central value of our result. We cannot presently resolve whether this shift is entirely explained by the different choice of scale.

[2] In this comparison, the contribution of the scale uncertainty to the error is not included.

O	$(a_\mu^{\text{hvp}})^{\text{SD}}$	$(a_\mu^{\text{hvp}})^{\text{ID}}$	$(a_\mu^{\text{hvp}})^{\text{LD}}$	a_μ^{hvp}
a_μ^{hvp}	68.76(0.21)(0.38)	236.60(0.79)(1.13)	423.2(4.2)(3.3)	728.6(4.3)(3.6)[5.5]
$a_\mu^{3,3}$	43.06(0.05)(0.21)	186.30(0.75)(1.08)	378.7(3.7)(3.1)	608.1(3.7)(3.3)[5.0]
$\frac{1}{3}a_\mu^{8,8}$	13.86(0.16)(0.78)	47.41(0.23)(0.29)	44.5(1.2)(1.1)	105.8(1.3)(1.4)[1.9]
$\frac{4}{9}a_\mu^{\text{c,c}}$	11.53(0.17)(0.23)	2.89(0.13)(0.03)	0.0141(4)(6)	14.4(0.2)(0.2)[0.3]
$\frac{1}{9}a_\mu^{\text{s,s}}$	9.07(0.01)(0.06)	27.68(0.18)(0.22)	17.73(0.17)(0.13)	54.5(0.3)(0.3)[0.4]
a_μ^{disc}	$1.3(2.6)(4.1)\cdot 10^{-3}$	−0.81(0.04)(0.08)	−15.3(1.2)(1.2)	−16.1(1.2)(1.2)[1.6]

Table 3. Contributions to a_μ^{hvp} in units of 10^{-10} in the infinite volume limit and isospin symmetric QCD as computed in [18, 22] and in this work. Note that the light-connected contribution that is conventionally quoted can be obtained from $\frac{10}{9}a_\mu^{3,3}$.

3.6 Full hadronic vacuum polarization contribution

Having computed $(a_\mu^{\text{hvp}})^{\text{LD}}$ in isoQCD, we can combine it with our results from [18] and [22] which, without the inclusion of isospin-breaking effects, read

$$(a_\mu^{\text{hvp}})^{\text{SD}} = 68.76(21)_{\text{stat}}(38)_{\text{syst}}[44]\,, \tag{3.10}$$
$$(a_\mu^{\text{hvp}})^{\text{ID}} = 236.60(79)_{\text{stat}}(1.13)_{\text{syst}}[1.38]\,. \tag{3.11}$$

We take the small correlation between the three observables into account when summing them. It is worth noting that we have used the intermediate scale setting quantity $\sqrt{t_0}$ from [36] in our computation of $(a_\mu^{\text{hvp}})^{\text{SD}}$. Since it has been determined from $f_{K\pi}$ using the exact same values for f_π and f_K as the ones that were used for $(a_\mu^{\text{hvp}})^{\text{ID}}$ and $(a_\mu^{\text{hvp}})^{\text{LD}}$, see appendix A, we can consistently combine the three windows. As our final result for a_μ^{hvp} in isospin-symmetric QCD as defined in appendix A, we quote

$$\begin{aligned}(a_\mu^{\text{hvp}})^{\text{isoQCD}} &= (a_\mu^{\text{hvp}})^{\text{SD}} + (a_\mu^{\text{hvp}})^{\text{ID}} + (a_\mu^{\text{hvp}})^{\text{LD}} \\ &= 728.6(4.3)_{\text{stat}}(3.6)_{\text{syst}}(0.8)_Q[5.6]\,.\end{aligned} \tag{3.12}$$

Similarly, the light-quark connected contribution, which dominates in the final result, is obtained by summing the results for the isovector contribution listed in the second row of Table 3 and multiplying by 10/9:

$$(a_\mu^{\text{hvp}})^{ud,\,\text{conn}} = 675.7(4.1)_{\text{stat}}(3.7)_{\text{syst}}[5.5]\,. \tag{3.13}$$

The electromagnetic and strong isospin-breaking corrections to these results are discussed in the next subsection.

We quote the results in eqs. (3.12) and (3.12) only in the f_π scheme because we did not determine the short and intermediate-distance window observables in the scheme of [14]. In their recent work [21] the RBC/UKQCD collaboration found only slight variations of these quantities between the BMW20 and their own scheme which, however, also employs m_Ω to set the scale.

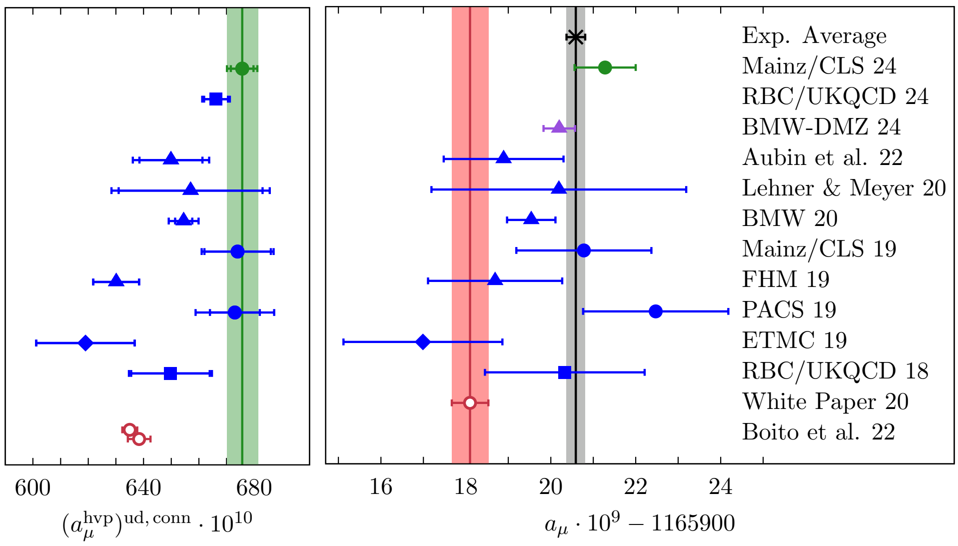

Figure 7. Compilation of lattice results for the light-quark connected contribution $a_\mu^{\rm hvp,ud}$ in isospin-symmetric QCD (left panel) and the total hadronic vacuum polarization contribution including isospin-breaking effects (right panel). Our results are represented by green circles and the green vertical band. Different discretizations of the quark action are denoted by circles (Wilson fermions) [34, 93], triangles (staggered fermions) [14, 15, 17, 24, 94], squares (domain wall fermions) [26, 88] and diamonds (twisted-mass Wilson fermions) [95]. Data-driven evaluations [1, 23] are represented as open red circles. In the right panel we show the current experimental average [12, 13, 96] as the grey vertical band, while the data-driven estimate from the 2020 White Paper is shown as the red band. The recent estimate by BMW-DMZ [24] is based on a combination of lattice and data-driven evaluations.

For all quark-connected flavour contributions we find excellent agreement with our previous work [34], albeit with significantly reduced uncertainties. In the case of the quark-disconnected contribution, we observe an upward shift that can be understood from the fact that only a small fraction of the current data set was available in [34] and an extrapolation to physical quark masses had to be performed. This increase in the quark-disconnected contribution is the main reason for the shift in the central value of $a_\mu^{\rm hvp}$ between [34] and this work that, however, is entirely within the uncertainty of [34].

In the left panel of figure 7 we compare our results for the light-quark connected contribution to other recent calculations. Our result for $a_\mu^{\rm hvp,ud}$ in our preferred scheme is compatible with the recent high-precision result of RBC/UKQCD [88]. There is a clear difference with the 2021 result of the BMW collaboration [14]. Unfortunately, BMW did not provide an updated value for this contribution in their most recent publication [24]. Assuming that the shift between their two results for $a_\mu^{\rm hvp}$ is mainly due to the light-connected contribution, the difference would be reduced accordingly. We note that our result is in clear tension with the evaluation from the data-driven dispersive approach in [23], regardless of whether the exclusive channel analysis of ref. [7] or [6] are used for the latter.

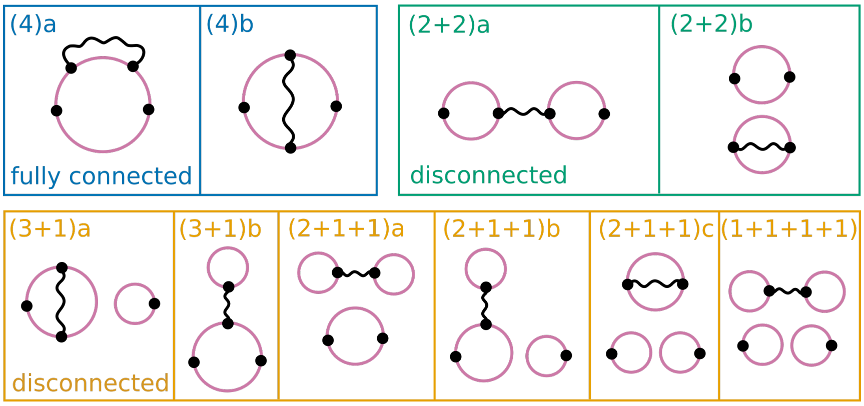

Figure 8. Overview of diagrams relevant for QED corrections.

3.7 Electromagnetic and strong isospin-breaking effects

In the following, we present the status of our calculations of the electromagnetic and strong isospin-breaking effects. While not complete, these calculations of some of the dominant diagrams already allow us to estimate the full correction without the associated uncertainty dominating the final error budget.

An overview of the diagrams involving internal photons is shown in figure 8. They are classified by the number and type of quark loops involved, with five classes identified: fully connected (4), and the classes (2+2), (3+1), (2+1+1), and (1+1+1+1). We have computed the connected part of the quark-mass insertion, as well as the connected QED diagrams (4)a and (4)b on the lattice, with the photon propagator evaluated in lattice regularization and infrared-regulated by removing the spatial zero mode on each timeslice [18, 22, 97–100]. These diagrams exclusively involve single-quark loops and form a UV-finite set.

In addition, we have computed the (2+2)a diagram [101], consisting of two (valence) quark loops connected by an internal photon, down to physical quark masses [102]. This diagram is UV-finite and has been computed with a photon propagator evaluated in the continuum and infinite volume using the coordinate-space approach from [103]. At small pion masses, it is found to be dominated by the charged pion loop. The observation that the $\pi\pi\gamma$ vertex only involves the isovector part of the electromagnetic current leads to two non-trivial homogeneous relations between the charged pion loop contributions to the various classes of diagrams. Neglecting the diagrams of the classes (2+1+1) and (1+1+1+1), one then arrives at the following partition of the charged pion loop among the diagrams [104],

$$a_\mu^{\pi\text{ loop},(4)} = \frac{34}{81} a_\mu^{\pi\text{ loop}}, \tag{3.14}$$

$$a_\mu^{\pi\text{ loop},(2+2)} = \frac{75}{81} a_\mu^{\pi\text{ loop}}, \tag{3.15}$$

$$a_\mu^{\pi\text{ loop},(3+1)} = -\frac{28}{81} a_\mu^{\pi\text{ loop}}. \tag{3.16}$$

The quantity $a_\mu^{\pi\text{ loop}}$ refers to the pion loop contribution, which, at the simplest level (i.e. without a pion form factor), could be estimated using scalar QED. The three coefficients

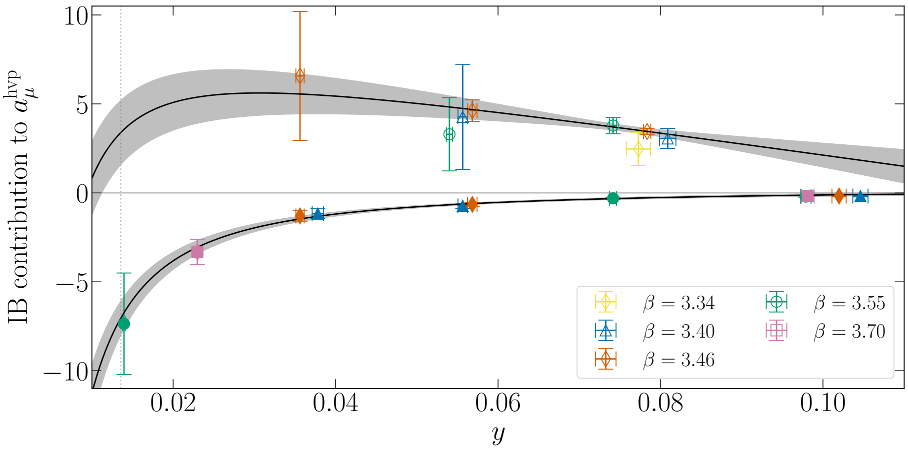

Figure 9. Chiral extrapolation of the isospin-breaking corrections to the physical pion mass based on eqs. (3.17) and (3.18). Open circles denote the fully connected (4) and filled diamonds the (2+2)a diagrams. The dotted vertical line denotes the physical value of y.

multiplying $a_\mu^{\pi\,\rm loop}$ sum to unity. This partition is used below.

We derive an estimate for the full QED correction by extrapolating simultaneously the single-quark-loop diagrams and the diagram (2+2)a; the remaining QED diagrams, consisting of at most two quark loops, are estimated based on the charged pion loop. The QED diagrams containing three or more quark loops are neglected. Indeed, they are $1/N_c^2$ suppressed compared to the fully connected diagrams. Both the BMW 2020 calculation [14] and the calculation of the light-by-light scattering contribution [104] found them to be small.

We use the superscript $1\gamma^*$ to denote contributions that contain one internal photon, including the required counterterms. These contributions are one-photon irreducible, i.e. they are part of the leading-order HVP contribution to a_μ in the standard nomenclature [1]. The charged pion loop, computed with a pion form factor of the vector-dominance form $M_V^2/(Q^2+M_V^2)$, has been found to behave like $1/m_\pi^3$ in the mass range of 135 to 300 MeV in a continuum calculation in scalar QED [102]. Based on this observation, our ansatz for a combined fit reads

$$a_\mu^{\mathrm{hvp}1\gamma^*,(4)} = \frac{34}{81}\frac{A}{m_\pi^3} + bm_\pi^2 + c + 0.22\,\log\frac{m_V^2}{m_\pi^2}\,, \tag{3.17}$$

$$a_\mu^{\mathrm{hvp}1\gamma^*,(2+2)\mathrm{a}} = \frac{50}{81}\frac{A}{m_\pi^3} + d\,, \tag{3.18}$$

where A, b, c and d are fit parameters. The logarithmic term corresponds to the neutral pion exchange contribution [103], including its 34/9 enhancement factor in the connected part [105].[3] The importance of this term is marginal.

To account for cutoff, finite-volume, and higher-order quark mass effects, we explore multiple fit models and combine them in a model average. Our fits extend the ansatz in

[3] In principle, the same contribution with a coefficient $-25/34 \cdot 0.22 = -0.16$ should be added to the (2+2)a diagram, however here we know that this contribution is largely compensated by the η and η' contribution [102, 106].

eqs. (3.17 – 3.18) by incorporating terms for cutoff effects and additional components to parameterize the pion mass dependence in the $a_\mu^{\mathrm{hvp1}\gamma^*,(2+2)\mathrm{a}}$ contribution. We also apply cuts on lattice spacing, pion mass, and Lm_π, and average over both local-local and local-conserved discretizations of the current for the fully connected contribution.

Figure 9 shows the chiral dependence of each of the two contributions in the continuum according to the best fit in the model average, represented by the black line and the gray uncertainty band. The open circles indicate data from fully connected diagrams, while the filled diamonds denote the (2+2)a contribution. The chiral dependence of the connected contribution near the physical pion mass, marked by the vertical line, is highly constrained by the curvature of the (2+2)a contribution. Our final estimate is given by[4]

$$a_\mu^{\mathrm{hvp1}\gamma^*} = -3.6(2.6)(1.1)(3.2)[4.2]. \tag{3.19}$$

The first two contributions to the total uncertainty are the statistical and systematic uncertainties as obtained from the model average. The third quoted error corresponds to the central value of the connected part $a_\mu^{\mathrm{hvp1}\gamma^*,(4)}$. We assign this uncertainty to our result to account for missing contributions from electrically charged sea quarks, as well as potential systematic effects from our parameterization based on the pion loop. Indeed, due to the observed cancellations between diagrams, in particular between the connected and the (2+2)a diagram, the size of the connected diagrams provides a conservative estimate of the total uncertainty.

Combining our evaluation of a_μ^{hvp} in isoQCD from eq. (3.12) with eq. (3.19), we obtain

$$a_\mu^{\mathrm{hvp}} = 724.9(5.0)_{\mathrm{stat}}(4.9)_{\mathrm{syst}}[7.0]\,, \tag{3.20}$$

for the full leading-order hadronic vacuum polarization contribution to a_μ. Our result is in tension with the data-driven evaluation of the 2020 White Paper at the level of $3.9\,\sigma$ but yields a SM prediction for the entire a_μ that agrees with the current experimental average.

4 Conclusion

We have performed a fully blinded, high-precision determination of the long-distance contribution, $(a_\mu^{\mathrm{hvp}})^{\mathrm{LD}}$, to the leading-order hadronic vacuum polarization contribution of the muon $g-2$. After combining the result with our previous calculations of the short- and intermediate-distance window observables [18, 22], we have obtained the entire HVP contribution in isospin-symmetric QCD with a total precision of 0.77% and a good balance between statistical and systematic uncertainties.

Compared to ref. [34], we have improved the precision of our estimate for a_μ^{hvp} in isospin-symmetric QCD by a factor 2.6. The key ingredients that allowed us to reach that level of precision were the addition of several high-statistics gauge ensembles at fine lattice spacing and close-to-physical quark mass, as well as the application of state-of-the-art noise reduction techniques to mitigate the exponential loss of signal in the long-distance regime.

[4]Ignoring the log term from the outset would have yielded an irrelevant shift of -0.2.

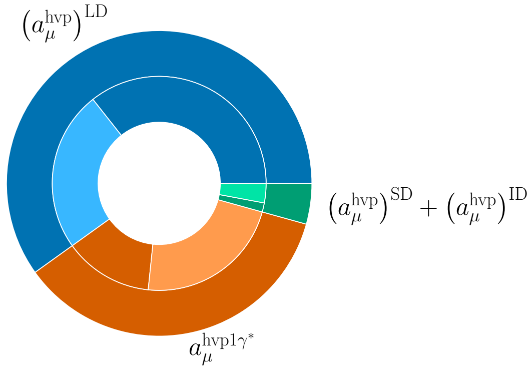

Figure 10. Squared uncertainty of our final estimate for $a_\mu^{\rm hvp}$ in eq. (3.20). Each of the three contributions can be divided into statistical (dark colours) and systematic uncertainties (light colours) that are displayed in the inner circle.

Furthermore, to quote a result for $a_\mu^{\rm hvp}$ that can be straightforwardly compared with the data-driven result, we have determined electromagnetic and strong isospin-breaking corrections. The resulting estimate, shown in eq. (3.20), has a relative precision of just under 1% and corroborates the strong tension observed between lattice calculations and data-driven evaluations derived from e^+e^- hadronic cross sections published prior to the result by CMD-3.

For our current result, the pie chart in figure 10 shows the squared uncertainties associated with the short, intermediate and long-distance window observables along with the isospin-breaking corrections. It is obvious that our efforts must focus on improving the precision for both the long-distance contribution and the isospin-breaking corrections. While the latter are small in absolute terms, they nevertheless make a sizeable contribution to the error.

While we still have a long way to go to reach our long-term goal of reducing the overall error to the level of about 0.2%, there is room for improvement: We are currently extending the set of gauge ensembles at fine lattice spacings, with a special focus on the ensemble F300 at physical value of the pion mass. This will allow us to further constrain mass-dependent and mass-independent cutoff effects in future analyses, which is crucial given that higher-order cutoff effects or modifications of the leading-order effects by non-zero anomalous dimensions cannot be excluded with our current data set. We also aim for improving the precision of our estimates for the isospin-breaking corrections by extending our lattice calculations beyond the electroquenched approximation. This includes the effect of isospin-breaking on scale setting, which is the subject of current investigations [107].

Acknowledgments

We thank Andrew Hanlon, Ben Hörz, Daniel Mohler, Colin Morningstar and Srijit Paul for the collaboration on the data generation and initial analysis for the spectral reconstruction of the isovector contribution. We also thank Volodymyr Biloshytskyi, Dominik Erb, Franziska Hagelstein and Vladimir Pascalutsa for an ongoing collaboration on computing electromagnetic corrections to hadronic vacuum polarization. Calculations for this project have been performed on the HPC clusters Clover and HIMster-II at Helmholtz Institute Mainz and Mogon-II and Mogon-NHR at Johannes Gutenberg-Universität (JGU) Mainz, on the HPC systems JUQUEEN and JUWELS and on the GCS Supercomputers HAZELHEN and HAWK at Höchstleistungsrechenzentrum Stuttgart (HLRS). The authors gratefully acknowledge the support of the Gauss Centre for Supercomputing (GCS) and the John von Neumann-Institut für Computing (NIC) projects HMZ21, HMZ23 and HINTSPEC at JSC, as well as projects GCS-HQCD and GCS-MCF300 at HLRS. We also gratefully acknowledge the scientific support and HPC resources provided by NHR-SW of Johannes Gutenberg-Universität Mainz (project NHR-Gitter). This work has been supported by Deutsche Forschungsgemeinschaft (German Research Foundation, DFG) through Project HI 2048/1-2 (Project No. 399400745) and through the Cluster of Excellence "Precision Physics, Fundamental Interactions and Structure of Matter" (PRISMA+ EXC 2118/1), funded within the German Excellence strategy (Project No. 39083149). This project has received funding from the European Union's Horizon Europe research and innovation programme under the Marie Skłodowska-Curie grant agreement No. 101106243. We are grateful to our colleagues in the CLS initiative for sharing ensembles. The `pyerrors` package [69] relies on `numpy` [108] and `autograd` [109]. Plots have been generated with `matplotlib` [110] and `gnuplot` [111].

A The hadronic scheme

Care has to be taken when working in isospin-symmetric QCD with respect to the definition of the physical point of the theory, since this definition is ambiguous. As soon as isospin-breaking effects are incorporated, this ambiguity is lifted. The exact definition of the scheme thus has an impact on the size of the isospin-breaking corrections. For a meaningful comparison of multiple independent calculations in isoQCD the exact definition of the physical point has to match, if the precision is of the order of these corrections.

In line with our calculations of the short and intermediate distance contributions to the HVP, we define our scheme for isoQCD via the conditions

$$m_\pi = (m_{\pi^0})_{\text{phys}}, \qquad 2m_K^2 - m_\pi^2 = (m_{K^+}^2 + m_{K^0}^2 - m_{\pi^+}^2)_{\text{phys}}, \tag{A.1}$$

corresponding to

$$m_\pi = 134.9768(5)\ \text{MeV}\,, \quad m_K = 495.011(10)\ \text{MeV}\,, \tag{A.2}$$

together with the pion decay constant in the isospin-symmetric theory [85, 112]

$$f_\pi = 130.56(14)\ \text{MeV}\,. \tag{A.3}$$

As outlined in section 2.5, we employ the combination $f_{K\pi}$ to correct for small deviations from the chiral trajectory on the CLS ensembles in our data set. Here, we employ the value $f_K = 157.2(5)$ MeV [85, 112] to define the physical point. It implies a ratio f_K/f_π

that is consistent with the latest lattice determinations [92, 113, 114]. As can be inferred from table 2, the dependence on f_K is largely suppressed with respect to the dependence on f_π. The charm quark, included in the partially quenched approximation, is fixed via the condition

$$m_{D_s} = 1968.47\,\mathrm{MeV}\,. \tag{A.4}$$

We parameterize the sea quark mass dependence of observables via the dimensionless combinations of eq. (2.20).

To be able to compare our result in isoQCD with that of [14], we also evaluate all observables in this work in the BMW20 scheme, defined by

$$m_\pi = 134.9768(5)\ \mathrm{MeV}\,, \quad M_{\mathrm{ss}} = 689.89(49)\,\mathrm{MeV}\,, \quad w_0 = 0.17236(70)\,\mathrm{fm}\,, \tag{A.5}$$

where M_{ss} is the meson with two mass-degenerate quarks with the mass of the strange quark and w_0 is computed from the gradient flowed gauge field [115]. As quark mass proxies in this scheme, we use the variables

$$\rho_2 = w_0^2 m_\pi^2 \propto m_\mathrm{l},\,, \qquad \rho_4 = w_0^2(m_\pi^2 + \frac{1}{2}M_{\mathrm{ss}}^2) \propto 2m_\mathrm{l} + m_\mathrm{s}\,, \tag{A.6}$$

and parameterize the lattice spacing with w_0/a as measured on our ensembles.

A.1 Results in the alternative scheme

To allow for comparisons in isoQCD without scheme ambiguity, we follow the approach of [21] and perform a full second analysis using the scheme of eq. (A.5). Compared to our preferred scheme, we note that the size of the cutoff effects in the contributions to $(a_\mu^{\mathrm{hvp}})^{\mathrm{LD}}$ is significantly larger and that these have a different sign compared to the case where we use f_π to make the muon mass in the QED kernel dimensionless. When performing the continuum extrapolations, fits that parameterize higher order lattice artefacts as well as mass-dependent cutoff effects are preferred over the other variations.

Due to the larger cutoff effects and the need to include terms that parameterize higher orders in the Symanzik expansion, we observe larger systematic and statistical uncertainties, when using w_0 to set the scale, compared to the f_π scheme. Our results in the BMW20 scheme are

$$(a_\mu^{3,3})^{\mathrm{LD}}_{\mathrm{BMW20}}(L_{\mathrm{ref}}) = 353.6(4.3)_{\mathrm{stat}}(5.2)_{\mathrm{syst}}(3.0)_{\mathrm{scale}}[7.3]\,, \tag{A.7}$$

$$\frac{1}{3}(a_\mu^{8,8})^{\mathrm{LD}}_{\mathrm{BMW20}}(L_{\mathrm{ref}}) = 42.5(1.8)_{\mathrm{stat}}(1.5)_{\mathrm{syst}}(0.4)_{\mathrm{scale}}[2.4]\,, \tag{A.8}$$

$$\frac{1}{9}(a_\mu^{s,s})^{\mathrm{LD}}_{\mathrm{BMW20}}(L_{\mathrm{ref}}) = 16.81(0.14)_{\mathrm{stat}}(0.23)_{\mathrm{syst}}(0.13)_{\mathrm{scale}}[0.29]\,, \tag{A.9}$$

$$(a_\mu^{\mathrm{hvp}})^{\mathrm{LD}}_{\mathrm{disc,BMW20}}(L_{\mathrm{ref}}) = -13.6(1.7)_{\mathrm{stat}}(1.6)_{\mathrm{syst}}(0.1)_{\mathrm{scale}}[2.4]\,. \tag{A.10}$$

Note that the contribution of the scale to the final error should not enter when comparing two results in the same scheme. The finite-volume correction in eq. (2.25) has been evaluated in the continuum limit and may be applied to correct the isovector and disconnected (with the appropriate scaling factor of $-1/9$) contributions.

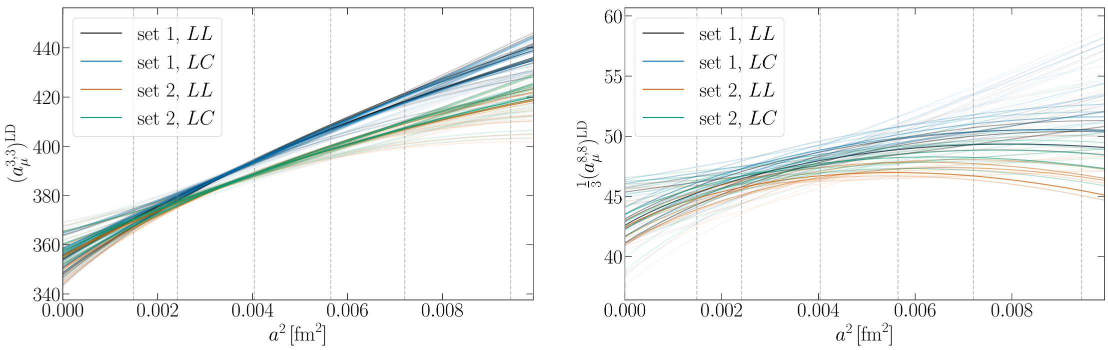

Figure 11. Continuum extrapolations using w_0/a to set the scale. *Right:* Approaches to the continuum limit for four sets of data based on the improvement schemes of set 1 and 2 and the LL and LC discretizations of the current based on a scan over fit models. Each line shows the result from one single fit and the opacity of the lines corresponds to the weight of the fit in the model average. Dashed vertical lines indicate the lattice spacings used in this work.

B The blinding strategy

To describe our blinding strategy, it is useful to recall the master formula for the time-momentum representation of $a_\mu^{\rm hvp}$ (see eq. (2.1))

$$a_\mu^{\rm hvp} = \left(\frac{\alpha}{\pi}\right)^2 \int_0^\infty dt\, G(t)\, \widetilde{K}(t; m_\mu), \tag{B.1}$$

where the kernel function $\widetilde{K}(t; m_\mu)$ is obtained by convoluting the momentum-space kernel $K(Q^2; m_\mu)$ defined in [116] with a time-dependent function [25]

$$\widetilde{K}(t; m_\mu) = 4\pi^2 \int_0^\infty dQ^2\, K(Q^2; m_\mu) \left[t^2 - \frac{4}{Q^2}\sin^2(Qt/2)\right]. \tag{B.2}$$

A simplified form of $K(Q^2; m_\mu)$ is given by

$$K(Q^2; m_\mu) = \frac{1}{m_\mu^2} \frac{\left(\sqrt{\frac{4m_\mu^2}{Q^2}+1}-1\right)^3}{4\left(\sqrt{\frac{4m_\mu^2}{Q^2}+1}+1\right)\sqrt{\frac{4m_\mu^2}{Q^2}+1}}. \tag{B.3}$$

Our approach to blinding is based on suitable modifications of the TMR kernel, which, when convoluted with (unmodified) numerical data for the current correlator, converge to the same result at the physical point, up to a multiplicative factor.

B.1 Modified kernel

One set of modified TMR kernels at a fixed value of t is defined via the function

$$\widetilde{K}_{\rm bld}(t; a; m; B; \boldsymbol{c}) = 4\pi^2 B \int_0^{(\pi/a)^2} dQ^2\, K(Q^2_{\rm lat}(Q,a); m) \left[t^2 - \frac{4}{Q^2_{\rm lat}(Q,a)}\sin^2(Qt/2)\right], \tag{B.4}$$

Set	B	s	ℓ[fm]	σ [fm^{-2}]	c_1	c_2
I	1.03628	+	0.80	−2.54	0.35	0.48
II	0.94348	−	0.73	+4.11	0.14	0.38
III	1.00971	−	0.84	+1.41	0.62	0.23
IV	0.96732	+	0.94	−0.92	0.45	0.55
V	1.02756	+	0.78	+1.82	0.26	0.69

Table 4. Parameters of the modified kernels I through V used for analyzing the lattice QCD data.

where

$$Q^2_{\rm lat}(Q,a) = c_2\Big(c_1\frac{1}{2a}\sin(2Qa) + (1-c_1)\frac{1}{a}\sin(Qa)\Big)^2 + (1-c_2)\Big(\frac{2}{a}\sin(Qa/2)\Big)^2. \qquad \text{(B.5)}$$

We restrict the value of c_1 and c_2 to

$$0 \le c_1 \le 1, \qquad 0 < c_2 < 0.7. \qquad \text{(B.6)}$$

Indeed, c_2 should not be chosen too large, to ensure that $Q_{\rm lat}$ remains large as $Q \to \pi/a$.

Concretely, we take the following steps: One "kernel set" is defined by a choice for the values of c_1, c_2, σ and ℓ. Then the quantities to be analyzed are

$$Ba_\mu^{\rm HVP,bld}(+1,\ell,\sigma,\boldsymbol{c}) = \Big(\frac{\alpha}{\pi}\Big)^2 \lim_{a\to 0}\int_0^\infty dt\, G(t,a)\, \widetilde{K}_{\rm bld}\Big(t; a\tanh\Big(\frac{t}{\ell}\Big); m_\mu(1+\sigma a^2); B; \boldsymbol{c}\Big). \qquad \text{(B.7)}$$

Reasonable values of the parameters are

$$0.75 \lesssim \ell \lesssim 1.0\,\text{fm}, \qquad -4 \lesssim \sigma[\text{fm}^{-2}] \lesssim 4. \qquad \text{(B.8)}$$

We also consider

$$\begin{aligned}&(2-B)a_\mu^{\rm HVP,bld}(-1,\ell,\sigma,\boldsymbol{c}) \qquad \text{(B.9)}\\ &= \Big(\frac{\alpha}{\pi}\Big)^2 \lim_{a\to 0}\int_0^\infty dt\, G(t,a)\, \Big(2\widetilde{K}(t;m_\mu) - \widetilde{K}_{\rm bld}\Big(t; a\tanh\Big(\frac{t}{\ell}\Big); m_\mu(1+\sigma a^2); B; \boldsymbol{c}\Big)\Big),\end{aligned}$$

which reverses the sign of the deviation of $\widetilde{K}_{\rm bld}$ from $\widetilde{K}$ at a given t. The test is based on the expectation that

$$a_\mu^{\rm hvp,bld}(s,\ell,\sigma,\boldsymbol{c}) = a_\mu^{\rm hvp}, \qquad \forall(s=\pm 1,\ell,\sigma,\boldsymbol{c}) \qquad \text{(B.10)}$$

at the physical point. The parameters of the five modified kernels used in the analysis of the lattice QCD data computed on the CLS ensembles are listed in table 4.

For the purpose of testing our blinding procedure, we generated five additional kernels (VI–X) that were used together with synthetic data for the vector correlator $G(t)$. For the latter we used the phenomenological model of [25] supplemented by an artificial pion mass and lattice spacing dependence. Indeed we were able to verify that the results obtained for kernels VI–X agreed with each other and the input in the continuum limit and at the physical pion mass.

C The vector correlator from low-mode averaging

The computation of an all-to-all estimator for the vector-vector correlation function, taking into account all possible pairs of source and sink, is prohibitively expensive in a large-scale lattice QCD computation. Low-mode averaging as introduced in ref. [43, 44] is based on the computation of the low eigenmodes of the Dirac operator to allow for an all-to-all sampling of the low mode contribution to the correlation function. If this contribution has a dominant weight in the long-distance tail, where the signal to noise problem hinders the reliable extraction of the correlator, it allows to significantly increase the available statistics in the most important region.

C.1 Low modes of the Dirac operator

We work with $\mathrm{O}(a)$ improved Wilson fermions, see ref. [27] for the exact definition of the Dirac operator D, and focus on the hermitian operator

$$Q = \gamma_5 D\,, \tag{C.1}$$

where we suppress the flavour index of the massive Dirac operator and assume to work with light quarks in the following. Its inverse Q^{-1} can be expressed via the eigenmodes of Q, denoted by v_i, via

$$Q^{-1} = \sum_{i=0}^{N} \frac{1}{\lambda_i}\, v_i \cdot v_i^\dagger\,, \tag{C.2}$$

where N is the dimension of the operator and λ_i are the real eigenvalues. The eigenmodes with the N_L smallest (in magnitude) eigenvalues are referred to as the "low modes". We define the projectors

$$\mathbf{P}_\mathrm{L} \equiv \sum_{i=0}^{N_\mathrm{L}} v_i \cdot v_i^\dagger\,, \qquad \mathbf{P}_\mathrm{H} \equiv \mathbf{1} - \mathbf{P}_\mathrm{L}\,. \tag{C.3}$$

on the space of the low modes and the corresponding orthogonal space. These allow to express D^{-1} via

$$D^{-1} = Q^{-1}(\mathbf{P}_\mathrm{L} + \mathbf{P}_\mathrm{H})\gamma_5 = \sum_{i=0}^{N} \frac{1}{\lambda_i}\, v_i \cdot v_i^\dagger \gamma_5 + Q^{-1}\mathbf{P}_\mathrm{H}\gamma_5\,, \tag{C.4}$$

and to split it into low and high mode contributions of Q.

C.2 Mesonic correlation functions

The computational challenge that is addressed in this appendix is the precise computation of a quark-connected, zero-momentum two-point function. After integrating out the fermions, we write

$$C_{\Gamma_A\Gamma_B}(x_0, y_0) = -\sum_{\mathbf{x},\mathbf{y}} \langle \mathrm{tr}\,[\Gamma_A S(x,y)\Gamma_B S(y,x)]\rangle^{\mathrm{gauge}}\,, \tag{C.5}$$

with the source and sink positions y and x, respectively, the trace tr that acts in colour and spin space and the gamma matrices Γ_A and Γ_B. In this work, these matrices are equal to γ_i or $\gamma_0\gamma_i$, were the latter combination is needed for the $\mathrm{O}(a)$ improvement of the current. Furthermore, we include the conserved (point-split) vector current in this work, but refrain from extending the notation for the sake of clarity in this appendix. The quark propagators S are defined via

$$\sum_y D(x,y)S(y,z) = \mathbf{1}\delta_{x,z}\,. \tag{C.6}$$

Based on eq. (C.4), each of the two propagators in eq. (C.5) can be exactly split into a low and a high mode contribution,

$$S(x,y) = \sum_{i=0}^{N} \frac{1}{\lambda_i}\, v_i(x)\cdot v_i^\dagger(y)\gamma_5 + S_{\mathrm{H}}(x,y)\,, \tag{C.7}$$

where $S_{\mathrm{H}}(x,y)$ is the propagator in the high mode space. Correspondingly, the correlation function can be decomposed into four terms which we denote as,

$$C_{\Gamma_A\Gamma_B}(x_0,y_0) = C^{(\mathrm{ee})}_{\Gamma_A\Gamma_B}(x_0,y_0) + C^{(\mathrm{re})}_{\Gamma_A\Gamma_B}(x_0,y_0) + C^{(\mathrm{er})}_{\Gamma_A\Gamma_B}(x_0,y_0) + C^{(\mathrm{rr})}_{\Gamma_A\Gamma_B}(x_0,y_0)\,. \tag{C.8}$$

The "eigen-eigen" contribution is purely built from the low modes of the Dirac operator such that both propagators can be expressed in terms of the low modes and the corresponding eigenvalues,

$$C^{(\mathrm{ee})}_{\Gamma_A\Gamma_B}(x_0,y_0) = -\sum_{i,j}^{N_{\mathrm{L}}}\sum_{\mathbf{x},\mathbf{y}} \frac{1}{\lambda_i\lambda_j}\left\langle [v_j^\dagger\gamma_5\Gamma_A v_i](x)[v_i^\dagger\gamma_5\Gamma_B v_j](y)\right\rangle\,. \tag{C.9}$$

Since the eigenmodes are lattice wide objects, this contribution can be computed in an all-to-all fashion without any further inversion of the Dirac operator. With the cost being purely due to contractions, it is possible to average over all source and sink positions.

The "rest-rest" contribution is defined only in the orthogonal subspace of the low mode space. It can be written as

$$C^{(\mathrm{rr})}_{\Gamma_A\Gamma_B}(x_0,y_0) = -\sum_{\mathbf{x},\mathbf{y}}\langle \mathrm{tr}\,[\Gamma_A S_{\mathrm{H}}(x,y)\Gamma_B S_{\mathrm{H}}(y,x)]\rangle\,, \tag{C.10}$$

where the only difference with respect to eq. (C.5) is the occurrence of the high mode propagator S_{H}. From a computational perspective, compared to a standard evaluation of the correlation function in eq. (C.5), the operator $\gamma_5 P_{\mathrm{H}}\gamma_5$ is applied to the source before each inversion of the Dirac operator. The correlation function can be sampled with standard methods.

The "rest-eigen" and "eigen-rest" contributions each contain a low and a high mode propagator and thus connect the two spaces. We can write

$$C^{(\mathrm{re})}_{\Gamma_A\Gamma_B}(x_0,y_0) = -\sum_{i}^{N_{\mathrm{L}}}\sum_{\boldsymbol{x},\boldsymbol{y}} \frac{1}{\lambda_i}\left\langle v_i^\dagger(x)\,\gamma_5\Gamma_A\, S_{\mathrm{H}}(x,y)\Gamma_B\, v_i(y)\right\rangle\,, \tag{C.11}$$

$$C^{(\mathrm{er})}_{\Gamma_A\Gamma_B}(x_0,y_0) = -\sum_{i}^{N_{\mathrm{L}}}\sum_{\boldsymbol{x},\boldsymbol{y}} \frac{1}{\lambda_i}\left\langle v_i^\dagger(y)\,\gamma_5\Gamma_B\, S_{\mathrm{H}}(y,x)\Gamma_A\, v_i(x)\right\rangle\,, \tag{C.12}$$

and notice that for $\Gamma_A = \Gamma_B$, the two functions are trivially related. The explicit inversion of the Dirac operator is performed in the high-mode space. We note that in some works, this contribution is not explicitly computed but instead estimated as bias correction, see e.g. [77]. As we will point out below, we find that the dedicated computation is vital for precision in our case.

C.3 Even-odd preconditioning

The dimension of the eigenproblem and with it the memory requirement of the computation can be reduced by a factor of two when considering the even-odd preconditioned Dirac operator $\hat{D}$, as pointed out for Wilson quarks in ref. [117]. We define the Schur complement of the asymmetric even-odd preconditioning of the hermitian Dirac operator [118],

$$\hat{Q} = Q_{\mathrm{ee}} - Q_{\mathrm{eo}} Q_{\mathrm{oo}}^{-1} Q_{\mathrm{oe}} \quad \text{with} \quad \hat{Q} = \gamma_5 \hat{D}\,, \tag{C.13}$$

and work with its eigenmodes, with support only on the even points of the lattice, to define the projectors

$$\hat{\mathbf{P}}_{\mathrm{L}} \equiv \sum_{i=0}^{N_{\mathrm{L}}} \hat{v}_i \cdot \hat{v}_i^\dagger\,, \qquad \hat{\mathbf{P}}_{\mathrm{H}} \equiv \mathbf{1} - \hat{\mathbf{P}}_{\mathrm{L}}\,, \tag{C.14}$$

such that the even-odd preconditioned Dirac operator can be expressed as

$$\hat{D}^{-1} = \hat{Q}^{-1}(\hat{\mathbf{P}}_{\mathrm{L}} + \hat{\mathbf{P}}_{\mathrm{H}})\gamma_5 = \sum_{i=0}^{N} \frac{1}{\hat{\lambda}_i}\, \hat{v}_i \cdot \hat{v}_i^\dagger \gamma_5 + \hat{Q}^{-1}\hat{\mathbf{P}}_{\mathrm{H}}\gamma_5\,. \tag{C.15}$$

For computing the correlation function of appendix C.2, the eigenmodes need to be projected back onto the space of the full Dirac operator. When even-odd preconditioning is used for the inversion of the Dirac operator, the projection operator can be inserted after projecting to the even lattice sites and before performing the inversion.

C.4 Computational details

Four tasks contribute dominantly to the effort of computing correlation functions with our implementation of LMA. These are the cost to compute a sufficiently large number of eigenmodes, the contraction for the "eigen-eigen" contribution, the inversion of the Dirac operator and the preceding projection to the high-mode space. In this subsection, we point out the specific setup that we have used in our computation after an extensive tuning towards optimal performance for the problem at hand.

Since the precise computation of the long-distance tail of the vector-vector correlation function is hindered by the signal-to-noise problem, this is the region where we want to make use of the all-to-all sampling of the "eigen-eigen" contribution. We have optimized the setup such that in this region, starting at a source-sink separation of about 1.5 fm, the central value and the variance of the full correlation function are dominated by the contribution of $C^{(\mathrm{ee})}$. This choice ensures that all information of the gauge fields is used to sample the long-distance tail and all noise stems from the fluctuations of the gauge field

Id	T [fm]	L [fm]	m_π [MeV]	N
C101	8.1	4.1	222(2)	384
D150	10.9	5.4	131(3)	608
D450	9.6	4.8	219(2)	608
D451	9.6	4.8	219(1)	608
D452	9.6	4.8	156(2)	640
D251	8.1	4.1	286(1)	480
D200	8.1	4.1	202(1)	480
D201	8.1	4.1	202(2)	480
E250	12.2	6.1	131(1)	800
J303	9.4	3.1	260(1)	288
J304	9.4	3.1	263(1)	288
E300	9.4	4.7	177(1)	704
F300	12.6	6.3	136(1)	800

Table 5. Overview of ensembles where low-mode averaging has been used to compute the isovector correlation function. The volume is given by $T \times L^3$, and m_π is the pion mass. N denotes the number of eigenmodes of $\hat{Q}$ that have been used in the computation.

configurations. It has a direct impact on the cost of the calculation because a sufficiently large number of eigenmodes has to be computed and the remaining correlation function, especially the mixed contributions, have to be known precisely enough not to spoil the signal. We note that a similar strategy has been chosen in ref. [14].

Solving the eigensystem. A large number of eigenmodes has to be computed to achieve low mode dominance in the long distance tail. This number varies significantly across the ensembles that have been included in this study. On the one hand, the number of modes with an eigenvalue below some fixed threshold scales with the lattice volume [119]. On the other hand, the dominance of the low modes is enhanced when the quark mass is lowered towards the chiral limit. In this work, these are competing effects since the volumes of the ensembles are increased as the pion mass is lowered.

One of the questions that determine whether LMA can be implemented cost-effectively, is if a sufficiently large number of eigenmodes can be computed with reasonable cost. We have observed that a first estimate for the number of eigenmodes can be found by requiring that the modulus of the largest eigenvalue of the low modes is of the order of the strange quark mass (or half of it when even-odd preconditioning is used). For the largest lattices in this work, at physical value of the pion mass, this amounts to computing 800 eigenmodes. Table 5 collects the number of eigenmodes that has been used for each of the ensembles where LMA has been applied.

For the solution of the hermitian eigenproblem, we utilize the Krylov-Schur algorithm in the implementation of the `SLEPc` package [120, 121] which relies on `PETSc` [122, 123]. When used on its own, we observe that a large number of iterations is needed to solve the eigensystem, resulting in a prohibitively large cost. The key ingredient for the efficient computation of the eigenmodes in this work is the use of a shift-and-invert spectral transformation: Instead of solving the equation

$$\hat{Q}\hat{v} = \hat{\lambda}\,\hat{v}\,, \tag{C.16}$$

we solve for

$$\hat{Q}^{-1}\hat{v} = \theta\,\hat{v} \quad \text{where} \quad \theta = 1/\hat{\lambda}\,. \tag{C.17}$$

This transformation has the effect of dramatically enhancing the convergence properties of the solver such that only a small number of iterations is necessary, between four and eight in our setup, with more than half of the modes converging in the first iteration. In turn, the Dirac operator has to be inverted for each of the vectors in the search space. We thus shift the work from the eigensolver of `SLEPc` to the deflated solver of the `openQCD` package [124, 125] and are able to profit from the physics informed optimizations of the solver. With a sufficiently well tuned setup, about 2 inversions have to be performed to compute one eigenmode. We have found this cost to scale linearly in the region of up to 1000 eigenmodes that we have explored in the context of this work.

Computing the eigen-eigen contribution. We have to compute the local-local and local-conserved vector-vector and vector-tensor currents for the full set of correlation functions that is used in this work. Efficient contraction routines are needed in order to keep the computational effort at a reasonable level and symmetries in the correlation function of eq. (C.9) can be utilize to reduce the number of contractions. On ensembles with antiperiodic boundary conditions, a full four-volume average can be performed. In contrast, on ensembles with open boundary conditions in the time direction, all pairs of source and sink where one of the two is in the boundary region has to be discarded from the average. The determination of the boundary region is performed at the stage of the analysis, based on the data that has been obtained for all source positions.

Computing the rest-rest contribution. The rest-rest contribution of eq. (C.10) can be computed with standard methods and we choose spin diluted stochastic time slice sources [126] for the computation. Since this contribution dominates at short distances only, it can be easily computed to the desired precision. To reduce the computational effort, we use the truncated solver method [127]. We perform low-precision solves on O(100) stochastic sources per configuration and correct for the small bias with a handful of high-precision solves. We note that the setup has been chosen such that the bias is completely negligible with respect to the statistical uncertainty for all relevant source-sink separations. A projection onto the high-mode space has to be performed before each inversion. On ensemble E250, the cost for one projection is about half of the cost of one truncated solve. Therefore, there is a limit to the computer time that can be gained with the truncated solves. It could be expected that the solves on the deflated sources are significantly faster than standard solves, given the large number of eigenmodes that is projected out. However, we find the improvement to be marginal when the `openQCD` solver, which is based on inexact deflation [124], is used to solve the Dirac equation.

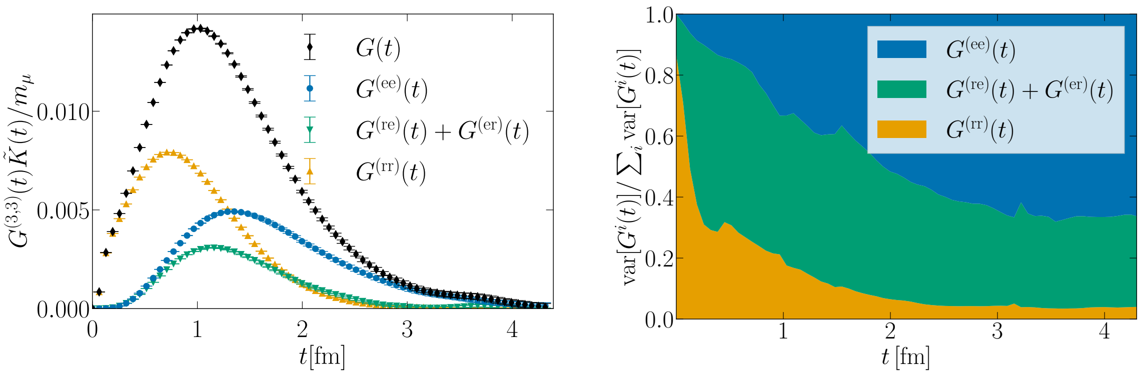

Figure 12. LMA computation on ensemble E250 at physical quark masses. *Left:* Integrand of $a_\mu^{(3,3)}$ (black) and the three contributions of the LMA computation. *Right:* Variances of the three contributions normalized by the variance of the full correlation function.

Computing the rest-eigen contribution. The rest-eigen and eigen-rest contributions of eqs. (C.11–C.12) provide a computational challenge, because a significant effort has to be made to compute it precisely enough such that its statistical uncertainty is small compared to that of the "eigen-eigen" contribution. As for the "rest-eigen" contribution, stochastic sources may be used for the computation. When inserted at the appropriate place, all Dirac structures can be computed from a single source, at the cost of contractions with all low modes. A sufficiently large number of sources has to be employed to reduce the stochastic noise. Due to the projection and contraction cost, the truncated solver method cannot be applied as efficiently in this case.

We have found the ansatz that has already been used in ref. [43] to be most effective for our purpose. It amounts to projecting an eigenmode to a specific source time slice before multiplying it with the appropriate Dirac matrix, projecting out the eigenmodes and inverting. The solution is then contracted with the eigenmode. This operation has to be performed for each Dirac matrix and eigenmode, leading to a very large number of inversions that makes up the largest fraction of the computational cost. To reduce the computational burden, we follow the approach of ref. [14] and perform truncated solves [127, 128]. The small bias, again negligible with respect to the statistical uncertainty, is corrected by computing high-precision solves on a small number of eigenmodes that are selected via Monte Carlo sampling.

This approach to compute the "rest-eigen" and "eigen-rest" contributions (which are related to each other) takes into account some of the all-to-all information of the eigenmodes. If performed for each source time slice, the result would indeed be an exact all-to-all estimator.

Synthesis Despite the significant computational effort, we have found low-mode averaging to be more efficient in computing the long-distance tail of the vector-vector correlation function than stochastic sampling, if the quark mass is small enough.[5] A bit surprisingly,

[5]For our ensembles with pion masses above 300 MeV, where the correlation function can be precisely computed with stochastic methods, LMA is not more efficient.

after optimizing the solution of the eigensystem and the contractions, the computation of the mixed contribution of low and high modes turned out to be the most costly part of our computation.

In figure 12 we show on the left hand side the integrand to compute the light-connected contribution to $a_\mu^{\rm hvp}$ on ensemble E250. The total, denoted by the black diamonds, is composed of the sum of the three coloured data sets. It is apparent that the low-mode contribution dominates for source-sink separations $t > 1.4\,\mathrm{fm}$. On the right hand panel of figure 12 we show the time dependent variance of each contribution, normalized by the sum of the three. Whereas the variance of the eigen-eigen contribution dominates the total in the long-distance regime, the variance of the rest-eigen contribution is non-negligible although the contribution to the isovector correlation function is small.

D $I = 1$ $\pi\pi$ scattering at physical pion mass

At relatively late times, we can further improve on the LMA correlator by replacing it with the spectral reconstruction of the isovector component. The LMA correlator, despite its precision, nevertheless suffers from an exponential loss in signal-to-noise; the reconstruction, in contrast, benefits from a constant signal-to-noise ratio and is therefore guaranteed to beat the LMA correlator eventually. For the E250 ensemble, the improvement from switching to the reconstructed current correlator occurs around $t \approx 2.5$ fm.

D.1 Measuring the finite-volume energies and matrix elements

To reconstruct the isovector current correlator $\langle J(t)J^\dagger(0)\rangle$, we employ the correlation functions [52]

$$\langle[\pi\pi](t)\,[\pi\pi]^\dagger(0)\rangle = Z^*_{\pi\pi}\,Z_{\pi\pi}e^{-E^{(0)}t} + \cdots\,, \tag{D.1}$$

$$\langle J(t)\,[\pi\pi]^\dagger(0)\rangle = Z^*_J\;\;Z_{\pi\pi}e^{-E^{(0)}t} + \cdots\,, \tag{D.2}$$

using a set of N different $\pi\pi$ interpolators $\{[\pi\pi]^{(1)},\cdots,[\pi\pi]^{(N)}\}$. The set of correlation functions formed from any two of these N interpolators forms an $N\times N$ correlation matrix which should, in principle, describe the lowest lying N states.

Given a set of interpolators describing a state of interest (in this case, two pions), we can form an optimized set of interpolators which approximately project onto particular excitations of that state by solving the associated generalized eigenvalue problem [129]

$$C(t)v_n(t,t_0) = \lambda_n(t,t_0)C(t_0)v_n(t,t_0)\,, \tag{D.3}$$

for the eigenvalues $\lambda_n(t,t_0)$ and eigenvectors $v_n(t,t_0)$, where $C(t)$ is a matrix of correlation functions formed by the outer product of a set of interpolators with itself.

If we consider the case of $\pi\pi$ scattering, then given a set of N interpolators $[\pi\pi]^{(n)}$, the solution to the generalized eigenvalue problem allows us to form a set of N optimized operators $[\Pi\,\Pi]^{(n)}(t;t_0) \equiv ([\pi\pi](t), v^{(n)}(t,t_0))$ describing N energy levels. Typically one then determines the energy levels either by fitting the principal correlators (the eigenvalues of the GEVP) to

$$\lambda^{(n)}(t,t_0) = e^{-E^{(n)}(t-t_0)} + \text{ h.o.}\,, \tag{D.4}$$

or by fitting the rotated correlators (formed from the eigenvectors of the GEVP) to

$$\langle [\Pi\,\Pi]^{(n)}(t;t_d,t_0)\,[\Pi\,\Pi]^{(n)\,\dagger}(0;t_d,t_0)\rangle = |Z^{(n)}|^2 e^{-E^{(n)}t} + \text{ h.o.}\,, \tag{D.5}$$

where t_d indicates that we have reused the eigenvalues from the solution to the GEVP at $t = t_d$ for all times.

The crucial part to either approach, however, is estimating what those higher-order corrections should be. Naively we expect that the corrections should not be worse than $\mathcal{O}(e^{-t\delta E})$ for an arbitrary choice of t_0, with $\delta E = \min_{n\neq m}|E_n - E_m|$ the smallest gap between energy levels in the spectrum [130]. However, the work of [131, 132] show that it is possible to do better than this provided one is clever about the asymptotic behaviour or the choice of GEVP parameters (for instance, by imposing the restriction $t_0/2 > t$).

As an example, let us consider the fits to the principal correlators. A result from [131] is that the higher-order corrections to (D.4) should be parameterized by

$$\epsilon_\lambda^{(n)}(t,t_0) \sim \mathcal{O}\left(e^{-(E^{(N)}-E^{(n)})t_0}e^{-E^{(n)}(t-t_0)}\right) + \mathcal{O}\left(e^{-E^{(N)}t}e^{+E^{(n)}t_0}\right)\,. \tag{D.6}$$

Therefore, for a fixed choice of t_0, a better choice of fit function for the principal correlators is given by

$$\lambda^{(n)}(t,t_0) \approx e^{-E^{(n)}(t-t_0)}\left[1 + A + Be^{-\Delta E^{(n)}t}\right]\,, \tag{D.7}$$

where $\Delta E^{(n)} \equiv E^{(N)} - E^{(n)} \geq \delta E^{(n)}$. This dependence on $\Delta E^{(n)}$ rather than $\delta E^{(n)}$ has two advantages: (1) since $\Delta E^{(n)}$ is larger, the correction is smaller; and (2) it is simpler to implement the constraint on $\Delta E^{(n)}$ in a simultaneous fit to all levels than the constraint on $\delta E^{(n)}$.

In this work we advocate the use of "sliding-pivot" fits to the effective masses and overlaps as motivated by the insights of [131, 132], in which the authors showed that the corrections to the effective energies and overlaps are described by

$$\begin{aligned}\epsilon_E^{(n)}(t,t_0) &= \mathcal{O}\left(e^{-\Delta E^{(n)}t}\right) + \mathcal{O}\left(e^{-2(\Delta E^{(n)}-\delta E^{(n)})t_0}e^{-\delta E^{(n)}t}\right) \\ &= \mathcal{O}\left(e^{-\Delta E^{(n)}t}\right) \qquad \text{when } t/2 \leq t_0 < t\,,\end{aligned} \tag{D.8}$$

$$\begin{aligned}\epsilon_Z^{(n)}(t,t_0) &= \mathcal{O}\left(e^{-\Delta E^{(n)}t_0}\right) + \mathcal{O}\left(e^{-(\Delta E^{(n)}-\delta E^{(n)})t_0}e^{-\delta E^{(n)}t}\right) \\ &= \mathcal{O}\left(e^{-\Delta E^{(n)}t_0}\right) \qquad \text{when } t/2 \leq t_0 < t\,.\end{aligned} \tag{D.9}$$

On the second line, we have shown the correction after restricting the choice of t_0 to the interval shown. Although both reduced expressions are similar, we note that the correction to the effective masses depends on t while the corrections to the effective overlaps depend on t_0.

Here we take this restriction on t_0 seriously: rather than fixing t_0 as is often done, we allow the parameter to vary with t, choosing the value of t_0 closest to (but greater than)

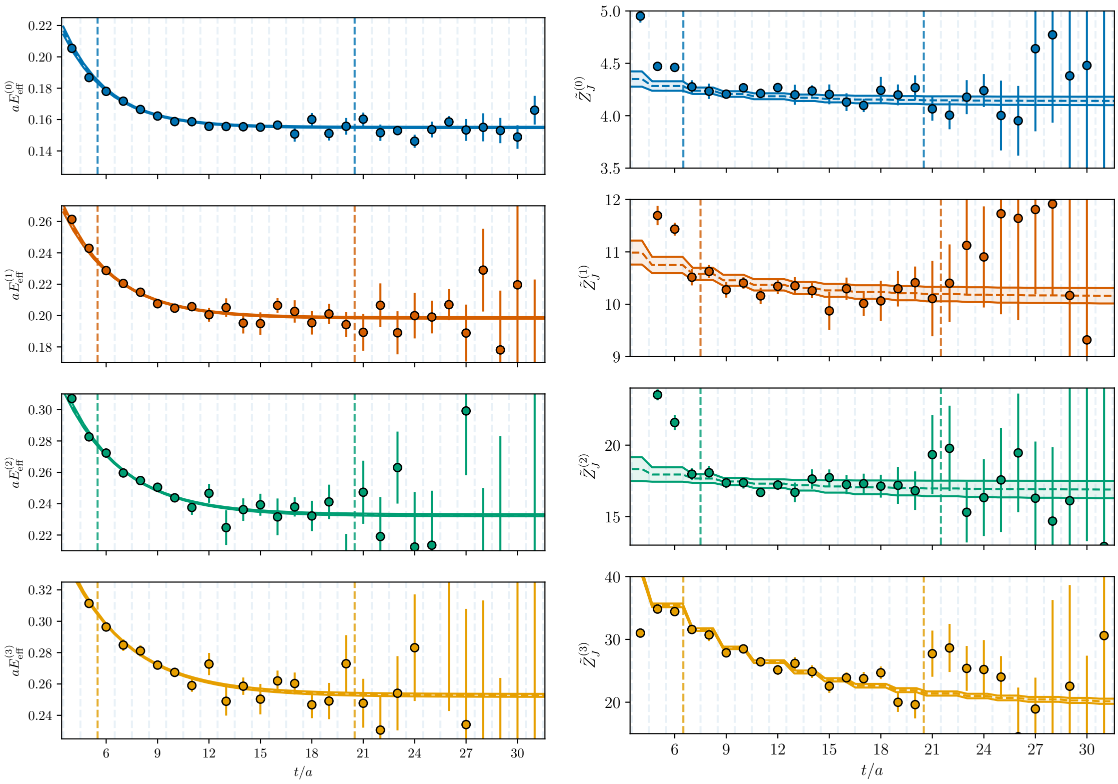

Figure 13. A representative fit to the first four effective masses (left) and effective matrix elements (right) on E250. The vertical bands denote the fit windows. For the effective matrix elements, we only fit every other data point, starting with the point right of the left-most dashed, vertical line.

$t/2$. We then construct/fit the effective masses per/to the following expressions:

$$E_{\text{eff}}^{(n)}(t) = \left\{ \log\left(\frac{\lambda^{(n)}(t-1,\lceil t/2\rceil)}{\lambda^{(n)}(t,\lceil t/2\rceil)}\right) \;\middle|\; t = 4,5,6,\dots \right\}, \tag{D.10}$$

$$E_{\text{eff}}^{(n)}(t) \approx E^{(n)}\left(1 + A_E^{(n)} e^{-\Delta E^{(n)} t}\right). \tag{D.11}$$

We simultaneously fit all N energy levels in order to better constrain the shared parameter $E^{(N)}$.

Similarly, the finite-volume matrix elements are determined by constructing the following effective quantities from the optimized mixed-current correlator $\langle J(t)\,[\Pi\,\Pi]^{(n)\dagger}(0)\rangle$ and two pion correlator $\langle [\Pi\,\Pi]^{(n)}(t)\,[\Pi\,\Pi]^{(n)\dagger}(0)\rangle$ and fitting them using the higher-order term described in (D.9),

$$\tilde{Z}_J^{(n)}(t) = \frac{\langle J(t)\,[\Pi\,\Pi]^{(n)\,\dagger}(0;\lceil t/2\rceil)\rangle}{\sqrt{\langle [\Pi\,\Pi]^{(n)}(t;\lceil t/2\rceil)\,[\Pi\,\Pi]^{(n)\,\dagger}(0;\lceil t/2\rceil)\rangle}} \left(\frac{\lambda^{(n)}(\lceil t/2\rceil+1,\lceil t/2\rceil)}{\lambda^{(n)}(\lceil t/2\rceil+2,\lceil t/2\rceil)}\right)^{t/2}, \tag{D.12}$$

$$\tilde{Z}_J^{(n)}(t) \approx Z_J^{(n)}\left(1 + A_Z^{(n)} e^{-\Delta E^{(n)}\lceil t/2\rceil}\right). \tag{D.13}$$

Again, we emphasize that the corrections to the effective matrix elements depend on t_0, not t.

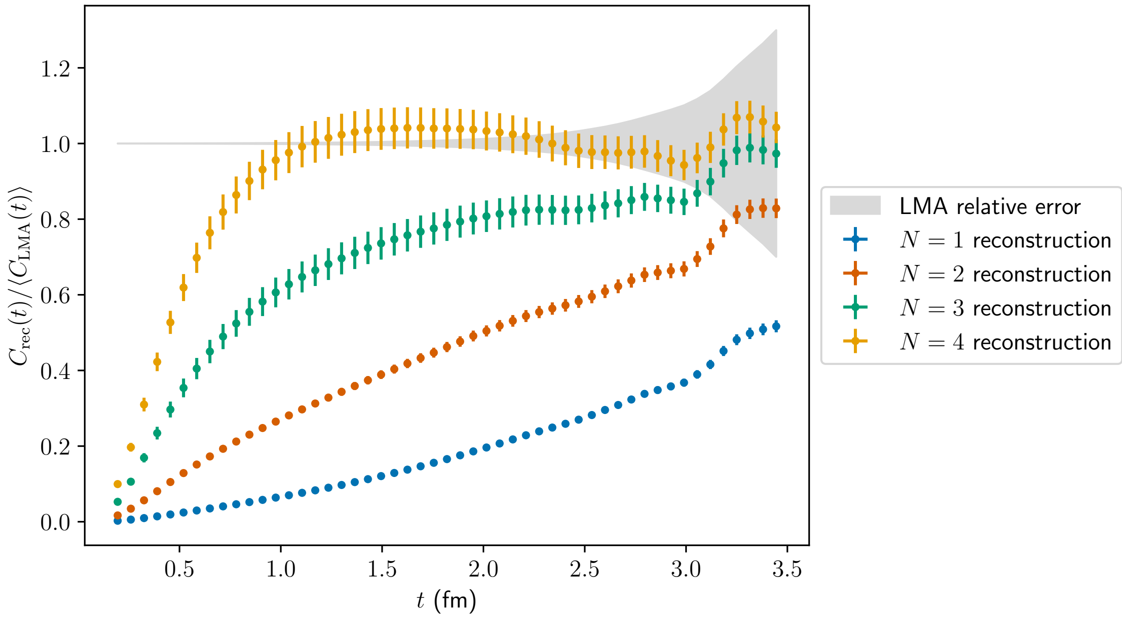

Figure 14. Saturation of the LMA correlator by the reconstructed correlator. The data points show the relative error of the reconstructed correlator if one normalizes by the LMA correlator instead of the reconstructed correlator. From the plot, one sees that the 4-state reconstruction saturates the LMA correlator around 1.2 fm, with the LMA correlator becoming less precise after 2.5 fm or so.

Although the fits to the effective matrix elements contain the energy levels as parameters, the fits to the effective masses are significantly more efficient at distinguishing these energy levels. Therefore, rather than simultaneously fit the effective masses and matrix elements, we first fit the energy levels using (D.11) before passing the posterior as a prior into the fit to the matrix elements using (D.13). Representative fits to the energy levels and matrix elements are shown in figure 13, respectively.

To minimize the systematic bias from our choice of fit windows ($t_{\rm min}, t_{\rm max}$) when fitting the effective masses and matrix elements, we vary the windows and calculate the posterior under a model-averaging framework using the Bayesian Akaike information criterion for the model weights [65, 133]. We find the model space for the spectrum fits to be strongly peaked around the representative fit shown in figure 13. In contrast, there is some noticeable spread among the fits to the effective matrix elements.

D.2 Transition Point and Gounaris-Sakurai Parameters

Rather than apply the bounding method [26, 50], we choose to replace the LMA correlator with the reconstructed correlator after some Euclidean distance. To identify the transition point, we first verify that the reconstructed correlator saturates the LMA correlator and then find the point for which the error for the reconstructed correlator is smaller than the LMA correlator (see figure 14).

We find that including four states is sufficient to saturate the LMA correlator. However, we note that including the states above the third excited state causes the reconstructed correlator to slightly overshoot the LMA correlator at the 1σ level. We therefore avoid including these states from the reconstruction for a few reasons: (1) after the third excited state, there is a pronounced decline in data quality, with the fourth excited state no longer exhibiting an exponential decay in the matrix element at the earliest times; (2) *a priori* we do not consider this overshooting to be physical but rather a systematic stemming from the difficulty of constraining higher-level states; and (3) including the fourth (or higher) states in our reconstruction has no bearing on the final result, as the contribution from these states has decayed-off before we reach the transition point near 2.5 fm.

Through this dedicated spectroscopy study, we are able to reduce the uncertainty on the physical pion mass ensemble E250 by a factor of two. An example application of the bounding method is shown in figure 1.

To compute the Gounaris-Sakurai parameters, we follow the procedure outlined in [52, 134]; the only notable deviation is the manner in which we calculate the finite-volume energy levels and matrix elements. After fitting the phase shifts, we find $g_{\rho\pi\pi} = 6.02(30)$ and $m_\rho/m_\pi = 5.76(9)$.

E Tables

This appendix contains tables 6 to 8 with detailed results for individual gauge ensembles.

id	am_π	am_K	af_π	t_0/a^2	y	z
A653	0.211 84(105)	0.211 84(105)	0.071 44(25)	2.173(7)	0.1110(13)	0.2448(37)
A654	0.166 33(131)	0.227 27(112)	0.067 25(25)	2.194(10)	0.0773(13)	0.2381(38)
H101	0.182 50(71)	0.182 50(71)	0.063 64(30)	2.847(6)	0.1046(9)	0.2274(27)
H102	0.153 83(80)	0.191 35(71)	0.060 44(31)	2.882(12)	0.0809(9)	0.2205(27)
H105	0.121 55(115)	0.202 23(85)	0.057 81(83)	2.886(9)	0.0559(11)	0.2198(29)
N101	0.121 20(56)	0.201 46(35)	0.057 73(35)	2.892(3)	0.0556(6)	0.2182(22)
C101	0.095 70(78)	0.205 84(44)	0.055 11(36)	2.913(5)	0.0378(6)	0.2137(22)
C102	0.096 40(87)	0.217 66(50)	0.055 07(46)	2.870(6)	0.0386(7)	0.2368(25)
D150	0.056 54(94)	0.208 35(35)	0.052 22(30)	2.944(4)	0.0150(5)	0.2049(20)
B450	0.160 81(50)	0.160 81(50)	0.056 85(20)	3.663(13)	0.1020(8)	0.2184(21)
S400	0.135 03(46)	0.170 22(41)	0.053 99(34)	3.692(8)	0.0781(6)	0.2145(20)
N452	0.135 46(30)	0.170 31(26)	0.054 62(15)	3.673(4)	0.0784(4)	0.2150(18)
N451	0.110 64(45)	0.178 22(26)	0.052 29(15)	3.682(7)	0.0568(5)	0.2133(18)
D450	0.083 46(51)	0.183 93(26)	0.049 77(14)	3.697(6)	0.0356(5)	0.2101(18)
D451	0.083 38(35)	0.193 82(16)	0.050 00(24)	3.665(3)	0.0359(3)	0.2311(18)
D452	0.059 32(59)	0.186 45(18)	0.047 58(15)	3.727(4)	0.0197(4)	0.2056(16)
H200	0.136 25(64)	0.136 25(64)	0.047 75(34)	5.151(33)	0.1000(11)	0.2125(24)
N202	0.134 36(32)	0.134 36(32)	0.048 46(13)	5.153(17)	0.0979(6)	0.2066(16)
N203	0.112 49(27)	0.143 95(23)	0.046 43(16)	5.147(7)	0.0742(4)	0.2064(15)
N200	0.092 21(29)	0.150 65(24)	0.044 20(18)	5.163(7)	0.0540(4)	0.2056(15)
D251	0.092 03(16)	0.150 41(12)	0.044 61(10)	5.164(5)	0.0538(3)	0.2050(14)
D200	0.065 02(28)	0.156 30(17)	0.042 37(20)	5.179(6)	0.0300(3)	0.2026(14)
D201	0.064 98(43)	0.163 08(24)	0.042 63(25)	5.137(8)	0.0302(4)	0.2191(16)
E250	0.042 32(23)	0.159 36(8)	0.040 18(12)	5.202(4)	0.0140(2)	0.2006(13)
N300	0.105 74(30)	0.105 74(30)	0.038 17(16)	8.560(32)	0.0981(7)	0.2072(17)
J307	0.105 47(42)	0.105 47(42)	0.037 85(17)	8.597(31)	0.0979(9)	0.2062(20)
N302	0.087 07(54)	0.113 63(46)	0.036 58(21)	8.526(25)	0.0721(9)	0.2064(22)
J306	0.086 90(19)	0.113 35(19)	0.036 53(13)	8.585(17)	0.0723(4)	0.2054(14)
J303	0.064 67(22)	0.119 63(19)	0.034 39(15)	8.618(14)	0.0447(4)	0.2027(14)
J304	0.065 61(20)	0.131 87(17)	0.034 18(12)	8.500(14)	0.0467(4)	0.2415(16)
E300	0.043 99(12)	0.124 02(9)	0.032 64(12)	8.614(5)	0.0230(2)	0.2020(12)
F300	0.033 81(23)	0.123 58(17)	0.031 68(23)	8.656(5)	0.0144(2)	0.1958(13)
J500	0.081 57(17)	0.081 57(17)	0.029 83(10)	13.964(31)	0.0941(6)	0.1966(14)
J501	0.065 90(23)	0.087 96(24)	0.028 55(15)	13.984(49)	0.0673(6)	0.1952(16)

Table 6. Pseudoscalar masses in lattice units, including finite-size corrections. Estimates of the gluonic observable t_0/a^2 and the two dimensionless variables ϕ_2 and ϕ_4 used in the extrapolation to the physical point.

	$(a_\mu^{3,3})^{\rm LD}$ - Set 2		$\frac{1}{3}(a_\mu^{8,8})^{\rm LD}$ - Set 2		$\frac{4}{9}(a_\mu^{\rm c,c})^{\rm LD}$ - Set 2	
id	*(LL)*	*(LC)*	*(LL)*	*(LC)*	*(LL)*	*(LC)*
A653	202.5(2.5)	206.2(2.6)	73.33(93)	74.56(94)	0.007 403(46)	0.006 947(33)
A654	216.3(3.4)	219.6(3.4)	51.94(82)	53.23(82)	0.008 36(12)	0.007 856(96)
H101	220.5(2.1)	222.7(2.1)	79.60(81)	80.31(80)	0.008 232(99)	0.007 294(81)
H102	236.1(3.8)	238.2(3.8)	64.4(1.1)	65.0(1.0)	0.008 81(14)	0.007 81(11)
H105	241.3(9.9)	243(10)	51.7(1.7)	52.3(1.6)	–	–
N101	238.7(4.1)	241.2(3.8)	49.49(77)	50.45(73)	0.009 73(10)	0.008 624(85)
C101	265.0(3.6)	266.9(4.0)	42.9(1.5)	44.1(1.5)	0.010 180(96)	0.009 021(77)
C102	254.9(6.3)	253.6(7.3)	38.7(1.6)	39.5(1.6)	–	–
D150	312.0(7.8)	313.4(7.8)	35.7(2.9)	36.7(3.0)	–	–
B450	225.0(2.8)	226.8(3.0)	80.8(1.0)	81.4(1.1)	0.008 530(77)	0.007 462(62)
S400	247.5(3.5)	248.7(3.5)	65.66(82)	66.19(81)	0.008 96(13)	0.007 94(11)
N452	243.6(2.1)	242.8(2.1)	66.00(47)	66.32(46)	–	–
N451	255.5(3.0)	256.5(3.0)	55.33(75)	55.85(73)	–	–
D450	270.6(2.3)	271.6(2.3)	45.6(1.1)	46.7(1.1)	0.010 836(95)	0.009 566(75)
D451	263.2(3.2)	264.4(3.1)	40.6(1.3)	41.2(1.2)	–	–
D452	299.1(4.4)	299.8(4.4)	38.0(2.0)	39.1(2.0)	0.011 301(94)	0.009 963(74)
H200	234.5(4.3)	235.0(4.3)	83.5(1.5)	83.7(1.5)	–	–
N202	239.7(2.9)	240.7(2.9)	85.9(1.1)	86.2(1.1)	0.008 85(13)	0.007 86(11)
N203	257.1(3.2)	257.8(3.2)	68.88(76)	69.12(76)	0.009 64(12)	0.008 55(10)
N200	265.5(4.6)	265.9(4.6)	56.5(1.1)	57.1(1.1)	0.010 523(95)	0.009 364(80)
D251	265.4(2.2)	265.8(2.2)	–	–	–	–
D200	289.2(3.0)	290.1(3.2)	46.1(1.6)	46.5(1.6)	0.011 620(98)	0.010 354(82)
D201	281.8(4.5)	282.3(4.5)	42.7(2.0)	43.4(2.0)	–	–
E250	341.9(3.2)	342.1(3.2)	37.9(2.2)	38.4(2.2)	0.012 067(86)	0.010 778(69)
N300	232.6(3.3)	232.7(3.2)	83.0(1.2)	83.0(1.2)	0.008 85(17)	0.008 10(15)
J307	252.9(3.9)	253.3(3.9)	90.7(1.5)	90.9(1.5)	–	–
N302	248.2(4.6)	248.9(4.7)	67.2(1.2)	67.4(1.2)	0.010 05(10)	0.009 213(88)
J306	258.4(5.1)	259.3(5.0)	–	–	–	–
J303	274.4(4.5)	274.9(4.5)	53.8(1.2)	54.1(1.2)	0.010 83(12)	0.010 04(11)
J304	262.2(4.7)	262.4(4.7)	45.6(1.4)	46.0(1.4)	–	–
E300	310.7(5.0)	311.4(5.0)	45.8(2.2)	46.3(2.1)	0.012 204(78)	0.011 226(71)
F300	350.4(9.7)	350.5(9.7)	–	–	–	–
J500	253.4(3.3)	254.6(4.0)	90.7(1.2)	91.1(1.4)	0.008 27(25)	0.007 80(23)
J501	265.5(6.1)	263.3(6.8)	68.3(1.4)	68.2(1.5)	–	–

Table 7. Values of the long-distance isovector, isoscalar and charm-connected contributions in units of 10^{-10}, for the local-local (LL) and for the local-conserved (LC) discretizations of the correlation function, as described in the main text. The finite-size correction to $(m_\pi L)^{\rm ref}$ has been applied to the isovector contribution.

id	HP&MLL	HP	Kaon	total
A653	−7.60(29)	−7.23(39)	–	−7.60(29)
A654	3.03(14)	2.66(15)	0.541(39)	3.57(14)
H101	−10.70(33)	−10.15(52)	–	−10.70(33)
H102	−4.27(25)	−4.14(19)	−1.186(90)	−5.45(27)
H105	4.07(27)	3.79(43)	0.322(24)	4.39(27)
N101	−6.59(20)	−6.36(28)	−0.336(22)	−6.93(20)
C101	−2.53(13)	−2.48(10)	−0.0230(13)	−2.56(13)
C102	−2.74(14)	−2.66(12)	−0.0163(20)	−2.75(14)
D150	11.33(98)	10.33(34)	0.000 941(42)	11.33(98)
B450	−7.21(21)	−6.89(35)	–	−7.21(21)
S400	−0.278(11)	−0.392(28)	−0.1142(94)	−0.392(14)
N452	−7.73(16)	−7.50(31)	−1.91(14)	−9.64(24)
N451	−5.54(12)	−5.39(19)	−0.363(24)	−5.90(13)
D450	−6.50(16)	−6.29(18)	−0.0357(19)	−6.54(16)
D451	−6.45(14)	−6.22(18)	−0.0218(12)	−6.47(14)
D452	6.85(38)	6.36(19)	0.002 96(14)	6.85(38)
H200	−0.793(34)	−0.974(57)	–	−0.793(34)
N202	−11.08(27)	−10.62(48)	–	−11.08(27)
N203	−5.64(14)	−5.49(24)	−1.39(10)	−7.04(17)
N200	−1.057(34)	−1.082(59)	−0.0842(57)	−1.141(34)
D251	−7.07(11)	−6.87(23)	−0.378(24)	−7.45(12)
D200	1.365(62)	1.267(59)	0.005 85(31)	1.371(62)
D201	1.329(55)	1.228(42)	0.004 05(21)	1.333(55)
E250	3.351(99)	3.164(58)	0.000 090 9(33)	3.351(99)
N300	−5.95(19)	−5.71(26)	–	−5.95(19)
J307	−11.95(50)	−11.45(79)	–	−11.95(50)
N302	0.857(43)	0.711(36)	0.227(18)	1.084(46)
J306	−5.81(23)	−5.65(35)	−1.340(96)	−7.15(25)
J303	1.317(39)	1.216(45)	0.0498(31)	1.367(40)
J304	0.794(23)	0.709(27)	0.015 57(99)	0.810(23)
E300	0.715(13)	0.651(15)	0.000 621(29)	0.716(13)
F300	−0.491(18)	−0.480(15)	−0.000 014 6(20)	−0.491(18)
J500	−7.65(32)	−7.27(32)	–	−7.65(32)
J501	0.572(22)	0.455(31)	0.1218(82)	0.694(24)

Table 8. Overview of finite-volume corrections to $(m_\pi L)^{\mathrm{ref}}$ using f_π to set the scale. The column denoted by HP&MLL gives the correction using the Hansen-Patella formalism for time separations smaller than t^* and using the MLL beyond that point. The column denoted by HP uses only the Hansen-Patella formalism. The column "Kaon" gives the correction from the Kaon, which is included in the pion correction on SU(3) symmetric ensembles. The total is computed by the sum of the columns "HP&MLL" and "Kaon" and enters the numbers for $(a_\mu^{3,3})^{\mathrm{LD}}$ in table 7. All uncertainties are statistical.

References

[1] T. Aoyama et al., *The anomalous magnetic moment of the muon in the Standard Model*, *Phys. Rept.* **887** (2020) 1 [2006.04822].

[2] M. Davier, A. Hoecker, B. Malaescu and Z. Zhang, *Reevaluation of the hadronic vacuum polarisation contributions to the Standard Model predictions of the muon $g-2$ and $\alpha(m_Z^2)$ using newest hadronic cross-section data*, *Eur. Phys. J. C* **77** (2017) 827 [1706.09436].

[3] A. Keshavarzi, D. Nomura and T. Teubner, *The muon $g-2$ and $\alpha(M_Z^2)$: a new data-based analysis*, *Phys. Rev. D* **97** (2018) 114025 [1802.02995].

[4] G. Colangelo, M. Hoferichter and P. Stoffer, *Two-pion contribution to hadronic vacuum polarization*, *JHEP* **02** (2019) 006 [1810.00007].

[5] M. Hoferichter, B.-L. Hoid and B. Kubis, *Three-pion contribution to hadronic vacuum polarization*, *JHEP* **08** (2019) 137 [1907.01556].

[6] M. Davier, A. Hoecker, B. Malaescu and Z. Zhang, *A new evaluation of the hadronic vacuum polarisation contributions to the muon anomalous magnetic moment and to $\alpha(m_Z^2)$*, *Eur. Phys. J. C* **80** (2020) 241 [1908.00921].

[7] A. Keshavarzi, D. Nomura and T. Teubner, *$g-2$ of charged leptons, $\alpha(M_Z^2)$, and the hyperfine splitting of muonium*, *Phys. Rev. D* **101** (2020) 014029 [1911.00367].

[8] H. Wittig, *Progress on $(g-2)_\mu$ from Lattice QCD*, in *57th Rencontres de Moriond on Electroweak Interactions and Unified Theories*, 6, 2023, 2306.04165.

[9] S. Kuberski, *Muon $g-2$: Lattice calculations of the hadronic vacuum polarization*, *PoS* **LATTICE2023** (2024) 125 [2312.13753].

[10] CMD-3 collaboration, F. V. Ignatov et al., *Measurement of the $e^+e^- \to \pi^+\pi^-$ cross section from threshold to 1.2 GeV with the CMD-3 detector*, *Phys. Rev. D* **109** (2024) 112002 [2302.08834].

[11] CMD-3 collaboration, F. V. Ignatov et al., *Measurement of the Pion Form Factor with CMD-3 Detector and its Implication to the Hadronic Contribution to Muon $(g-2)$*, *Phys. Rev. Lett.* **132** (2024) 231903 [2309.12910].

[12] Muon $g-2$ collaboration, B. Abi et al., *Measurement of the Positive Muon Anomalous Magnetic Moment to 0.46 ppm*, *Phys. Rev. Lett.* **126** (2021) 141801 [2104.03281].

[13] Muon $g-2$ collaboration, D. P. Aguillard et al., *Measurement of the Positive Muon Anomalous Magnetic Moment to 0.20 ppm*, *Phys. Rev. Lett.* **131** (2023) 161802 [2308.06230].

[14] S. Borsanyi et al., *Leading hadronic contribution to the muon magnetic moment from lattice QCD*, *Nature* **593** (2021) 51 [2002.12347].

[15] C. Lehner and A. S. Meyer, *Consistency of hadronic vacuum polarization between lattice QCD and the R-ratio*, *Phys. Rev. D* **101** (2020) 074515 [2003.04177].

[16] χQCD collaboration, G. Wang, T. Draper, K.-F. Liu and Y.-B. Yang, *Muon g-2 with overlap valence fermions*, *Phys. Rev. D* **107** (2023) 034513 [2204.01280].

[17] C. Aubin, T. Blum, M. Golterman and S. Peris, *Muon anomalous magnetic moment with staggered fermions: Is the lattice spacing small enough?*, *Phys. Rev. D* **106** (2022) 054503 [2204.12256].

[18] M. Cè, A. Gérardin, G. von Hippel, R. J. Hudspith, S. Kuberski, H. B. Meyer et al., *Window observable for the hadronic vacuum polarization contribution to the muon g-2 from lattice QCD*, Phys. Rev. D **106** (2022) 114502 [2206.06582].

[19] Extended Twisted Mass collaboration, C. Alexandrou et al., *Lattice calculation of the short and intermediate time-distance hadronic vacuum polarization contributions to the muon magnetic moment using twisted-mass fermions*, Phys. Rev. D **107** (2023) 074506 [2206.15084].

[20] Fermilab Lattice, HPQCD, MILC collaboration, A. Bazavov et al., *Light-quark connected intermediate-window contributions to the muon g-2 hadronic vacuum polarization from lattice QCD*, Phys. Rev. D **107** (2023) 114514 [2301.08274].

[21] RBC, UKQCD collaboration, T. Blum et al., *Update of Euclidean windows of the hadronic vacuum polarization*, Phys. Rev. D **108** (2023) 054507 [2301.08696].

[22] S. Kuberski, M. Cè, G. von Hippel, H. B. Meyer, K. Ottnad, A. Risch et al., *Hadronic vacuum polarization in the muon $g-2$: the short-distance contribution from lattice QCD*, JHEP **03** (2024) 172 [2401.11895].

[23] D. Boito, M. Golterman, K. Maltman and S. Peris, *Data-based determination of the isospin-limit light-quark-connected contribution to the anomalous magnetic moment of the muon*, Phys. Rev. D **107** (2023) 074001 [2211.11055].

[24] A. Boccaletti et al., *High precision calculation of the hadronic vacuum polarisation contribution to the muon anomaly*, 2407.10913.

[25] D. Bernecker and H. B. Meyer, *Vector Correlators in Lattice QCD: Methods and applications*, Eur. Phys. J. A **47** (2011) 148 [1107.4388].

[26] RBC, UKQCD collaboration, T. Blum, P. A. Boyle, V. Gülpers, T. Izubuchi, L. Jin, C. Jung et al., *Calculation of the hadronic vacuum polarization contribution to the muon anomalous magnetic moment*, Phys. Rev. Lett. **121** (2018) 022003 [1801.07224].

[27] M. Bruno et al., *Simulation of QCD with N_f = 2 + 1 flavors of non-perturbatively improved Wilson fermions*, JHEP **02** (2015) 043 [1411.3982].

[28] G. S. Bali, E. E. Scholz, J. Simeth and W. Söldner, *Lattice simulations with $N_f = 2+1$ improved Wilson fermions at a fixed strange quark mass*, Phys. Rev. D **94** (2016) 074501 [1606.09039].

[29] J. Bulava and S. Schaefer, *Improvement of $N_f = 3$ lattice QCD with Wilson fermions and tree-level improved gauge action*, Nucl. Phys. B **874** (2013) 188 [1304.7093].

[30] M. Clark and A. Kennedy, *Accelerating dynamical fermion computations using the rational hybrid Monte Carlo (RHMC) algorithm with multiple pseudofermion fields*, Phys. Rev. Lett. **98** (2007) 051601 [hep-lat/0608015].

[31] M. Lüscher and S. Schaefer, *Lattice QCD with open boundary conditions and twisted-mass reweighting*, Comput. Phys. Commun. **184** (2013) 519 [1206.2809].

[32] D. Mohler and S. Schaefer, *Remarks on strange-quark simulations with Wilson fermions*, Phys. Rev. D **102** (2020) 074506 [2003.13359].

[33] S. Kuberski, *Low-mode deflation for twisted-mass and RHMC reweighting in lattice QCD*, Comput. Phys. Commun. **300** (2024) 109173 [2306.02385].

[34] A. Gérardin, M. Cè, G. von Hippel, B. Hörz, H. B. Meyer, D. Mohler et al., *The leading hadronic contribution to $(g-2)_\mu$ from lattice QCD with $N_\mathrm{f}=2+1$ flavours of $O(a)$ improved Wilson quarks*, *Phys. Rev. D* **100** (2019) 014510 [1904.03120].

[35] M. Cè, A. Gérardin, G. von Hippel, H. B. Meyer, K. Miura, K. Ottnad et al., *The hadronic running of the electromagnetic coupling and the electroweak mixing angle from lattice QCD*, *JHEP* **08** (2022) 220 [2203.08676].

[36] B. Strassberger et al., *Scale setting for CLS 2+1 simulations*, *PoS* **LATTICE2021** (2022) 135 [2112.06696].

[37] RQCD collaboration, G. S. Bali, S. Collins, P. Georg, D. Jenkins, P. Korcyl, A. Schäfer et al., *Scale setting and the light baryon spectrum in $N_f = 2+1$ QCD with Wilson fermions*, *JHEP* **05** (2023) 035 [2211.03744].

[38] A. Gérardin, T. Harris and H. B. Meyer, *Nonperturbative renormalization and $O(a)$-improvement of the nonsinglet vector current with $N_f = 2+1$ Wilson fermions and tree-level Symanzik improved gauge action*, *Phys. Rev. D* **99** (2019) 014519 [1811.08209].

[39] ALPHA collaboration, J. Heitger and F. Joswig, *The renormalised* $\mathrm{O}(a)$ *improved vector current in three-flavour lattice QCD with Wilson quarks*, *Eur. Phys. J. C* **81** (2021) 254 [2010.09539].

[40] RQCD collaboration, G. S. Bali, S. Collins, S. Heybrock, M. Löffler, R. Rödl, W. Söldner et al., *Octet baryon isovector charges from Nf=2+1 lattice QCD*, *Phys. Rev. D* **108** (2023) 034512 [2305.04717].

[41] T. Harris and H. B. Meyer, to be published.

[42] P. Fritzsch, *Mass-improvement of the vector current in three-flavor QCD*, *JHEP* **06** (2018) 015 [1805.07401].

[43] L. Giusti, P. Hernandez, M. Laine, P. Weisz and H. Wittig, *Low-energy couplings of QCD from current correlators near the chiral limit*, *JHEP* **04** (2004) 013 [hep-lat/0402002].

[44] T. A. DeGrand and S. Schaefer, *Improving meson two point functions in lattice QCD*, *Comput. Phys. Commun.* **159** (2004) 185 [hep-lat/0401011].

[45] ETM collaboration, K. Jansen, C. Michael and C. Urbach, *The eta-prime meson from lattice QCD*, *Eur. Phys. J. C* **58** (2008) 261 [0804.3871].

[46] L. Giusti, T. Harris, A. Nada and S. Schaefer, *Frequency-splitting estimators of single-propagator traces*, *Eur. Phys. J. C* **79** (2019) 586 [1903.10447].

[47] A. Stathopoulos, J. Laeuchli and K. Orginos, *Hierarchical probing for estimating the trace of the matrix inverse on toroidal lattices*, 1302.4018.

[48] V. Gülpers, G. von Hippel and H. Wittig, *Scalar pion form factor in two-flavor lattice QCD*, *Phys. Rev. D* **89** (2014) 094503 [1309.2104].

[49] C. Lehner, *The hadronic vacuum polarization contribution to the muon anomalous magnetic moment*, in *RBRC Workshop on Lattice Gauge Theories*, 2016, https://indico.bnl.gov/event/1628/contributions/2819/.

[50] S. Borsanyi, Z. Fodor, T. Kawanai, S. Krieg, L. Lellouch, R. Malak et al., *Slope and curvature of the hadronic vacuum polarization at vanishing virtuality from lattice QCD*, *Phys. Rev. D* **96** (2017) 074507 [1612.02364].

[51] M. Della Morte, A. Francis, V. Gülpers, G. Herdoíza, G. von Hippel, H. Horch et al., *The hadronic vacuum polarization contribution to the muon $g-2$ from lattice QCD*, *JHEP* **10** (2017) 020 [1705.01775].

[52] C. Andersen, J. Bulava, B. Hörz and C. Morningstar, *The $I=1$ pion-pion scattering amplitude and timelike pion form factor from $N_\mathrm{f}=2+1$ lattice QCD*, *Nucl. Phys. B* **939** (2019) 145 [1808.05007].

[53] S. Paul, A. D. Hanlon, B. Hörz, D. Mohler, C. Morningstar and H. Wittig, *I=1 π-π scattering at the physical point*, *PoS* **LATTICE2021** (2022) 551 [2112.07385].

[54] S. Paul, A. D. Hanlon, B. Hörz, D. Mohler, C. Morningstar and H. Wittig, *The long-distance behaviour of the vector-vector correlator from $\pi\pi$ scattering*, *PoS* **LATTICE2022** (2023) 073.

[55] G. Colangelo, M. Hoferichter, B. Kubis, M. Niehus and J. R. de Elvira, *Chiral extrapolation of hadronic vacuum polarization*, *Phys. Lett. B* **825** (2022) 136852 [2110.05493].

[56] N. Husung, P. Marquard and R. Sommer, *Asymptotic behavior of cutoff effects in Yang–Mills theory and in Wilson's lattice QCD*, *Eur. Phys. J. C* **80** (2020) 200 [1912.08498].

[57] N. Husung, P. Marquard and R. Sommer, *The asymptotic approach to the continuum of lattice QCD spectral observables*, *Phys. Lett. B* **829** (2022) 137069 [2111.02347].

[58] N. Husung, *Lattice artifacts of local fermion bilinears up to* $\mathrm{O}(a^2)$, 2409.00776.

[59] G. Colangelo, S. Dürr and C. Haefeli, *Finite volume effects for meson masses and decay constants*, *Nucl. Phys. B* **721** (2005) 136 [hep-lat/0503014].

[60] M. Dalla Brida, T. Korzec, S. Sint and P. Vilaseca, *High precision renormalization of the flavour non-singlet Noether currents in lattice QCD with Wilson quarks*, *Eur. Phys. J. C* **79** (2019) 23 [1808.09236].

[61] RQCD collaboration, G. S. Bali, V. Braun, S. Collins, A. Schäfer and J. Simeth, *Masses and decay constants of the η and η' mesons from lattice QCD*, *JHEP* **08** (2021) 137 [2106.05398].

[62] J. Gasser and H. Leutwyler, *Chiral Perturbation Theory: Expansions in the Mass of the Strange Quark*, *Nucl. Phys. B* **250** (1985) 465.

[63] Baikov, P. A. and Chetyrkin, K. G. and Kühn, J. H., *Five-Loop Running of the QCD coupling constant*, *Phys. Rev. Lett.* **118** (2017) 082002 [1606.08659].

[64] ALPHA collaboration, M. Bruno, M. Dalla Brida, P. Fritzsch, T. Korzec, A. Ramos, S. Schaefer et al., *QCD Coupling from a Nonperturbative Determination of the Three-Flavor Λ Parameter*, *Phys. Rev. Lett.* **119** (2017) 102001 [1706.03821].

[65] W. I. Jay and E. T. Neil, *Bayesian model averaging for analysis of lattice field theory results*, *Phys. Rev. D* **103** (2021) 114502 [2008.01069].

[66] H. Akaike, *Information theory and an extension of the maximum likelihood principle*, in *Springer Series in Statistics*, p. 199, Springer New York, (1998), 10.1007/978-1-4612-1694-0_15.

[67] ALPHA collaboration, U. Wolff, *Monte Carlo errors with less errors*, *Comput. Phys. Commun.* **156** (2004) 143 [hep-lat/0306017].

[68] A. Ramos, *Automatic differentiation for error analysis of Monte Carlo data*, *Comput. Phys. Commun.* **238** (2019) 19 [1809.01289].

[69] F. Joswig, S. Kuberski, J. T. Kuhlmann and J. Neuendorf, *pyerrors: A python framework for error analysis of Monte Carlo data*, *Comput. Phys. Commun.* **288** (2023) 108750 [2209.14371].

[70] M. T. Hansen and A. Patella, *Finite-volume effects in $(g-2)_\mu^{HVP,LO}$*, *Phys. Rev. Lett.* **123** (2019) 172001 [1904.10010].

[71] M. T. Hansen and A. Patella, *Finite-volume and thermal effects in the leading-HVP contribution to muonic $(g-2)$*, *JHEP* **10** (2020) 029 [2004.03935].

[72] H. B. Meyer, *Lattice QCD and the Timelike Pion Form Factor*, *Phys. Rev. Lett.* **107** (2011) 072002 [1105.1892].

[73] M. Della Morte and A. Jüttner, *Quark disconnected diagrams in chiral perturbation theory*, *JHEP* **1011** (2010) 154 [1009.3783].

[74] A. Francis, B. Jäger, H. B. Meyer and H. Wittig, *A new representation of the Adler function for lattice QCD*, *Phys. Rev. D* **88** (2013) 054502 [1306.2532].

[75] D. Djukanovic, A. D. Hanlon, B. Hörz, S. Kuberski, H. B. Meyer, N. Miller et al., *The pion form factor on an $N_f = 2+1$ $O(a)$-improved Wilson fermions physical point ensemble*, in preparation.

[76] Particle Data Group collaboration, S. Navas et al., *Review of particle physics*, *Phys. Rev. D* **110** (2024) 030001.

[77] C. Aubin, T. Blum, C. Tu, M. Golterman, C. Jung and S. Peris, *Light quark vacuum polarization at the physical point and contribution to the muon $g-2$*, *Phys. Rev. D* **101** (2020) 014503 [1905.09307].

[78] SND collaboration, M. N. Achasov et al., *Study of the process $e^+e^- \to \omega\pi^0 \to \pi^+\pi^-\pi^0\pi^0$ in the energy range 1.05–2.00 GeV with SND*, *Phys. Rev. D* **108** (2023) 092012 [2309.00280].

[79] J. Wess and B. Zumino, *Consequences of anomalous Ward identities*, *Phys. Lett. B* **37** (1971) 95.

[80] E. Witten, *Global Aspects of Current Algebra*, *Nucl. Phys. B* **223** (1983) 422.

[81] H. Yan, M. Garofalo, M. Mai, U.-G. Meißner and C. Urbach, *The ω-meson from lattice QCD*, 2407.16659.

[82] M. Bruno, T. Izubuchi, C. Lehner and A. S. Meyer, *Exclusive Channel Study of the Muon HVP*, *PoS* **LATTICE2019** (2019) 239 [1910.11745].

[83] MILC collaboration, A. Bazavov et al., *Results for light pseudoscalar mesons*, *PoS* **LATTICE2010** (2010) 074 [1012.0868].

[84] R. J. Dowdall, C. T. H. Davies, G. P. Lepage and C. McNeile, *V_{us} from π and K decay constants in full lattice QCD with physical u, d, s and c quarks*, *Phys. Rev. D* **88** (2013) 074504 [1303.1670].

[85] Flavour Lattice Averaging Group (FLAG) collaboration, Y. Aoki et al., *FLAG Review 2021*, *Eur. Phys. J. C* **82** (2022) 869 [2111.09849].

[86] ALPHA collaboration, M. Bruno, J. Finkenrath, F. Knechtli, B. Leder and R. Sommer, *Effects of Heavy Sea Quarks at Low Energies*, *Phys. Rev. Lett.* **114** (2015) 102001 [1410.8374].

[87] ALPHA collaboration, F. Knechtli, T. Korzec, B. Leder and G. Moir, *Power corrections from decoupling of the charm quark*, *Phys. Lett. B* **774** (2017) 649 [1706.04982].

[88] RBC, UKQCD collaboration, T. Blum et al., *The long-distance window of the hadronic vacuum polarization for the muon $g-2$*, 2410.20590.

[89] R. J. Hudspith, M. F. M. Lutz and D. Mohler, *Precise Omega baryons from lattice QCD*, 2404.02769.

[90] S. Lingscheid, "Nucleon mass and scale setting in lattice QCD using O(a) improved $N_f = 2+1$ Wilson fermions." Master Thesis, Johannes Gutenberg University Mainz, 2024.

[91] MILC collaboration, A. Bazavov et al., *Gradient flow and scale setting on MILC HISQ ensembles*, *Phys. Rev. D* **93** (2016) 094510 [1503.02769].

[92] Extended Twisted Mass collaboration, C. Alexandrou et al., *Ratio of kaon and pion leptonic decay constants with $N_f = 2+1+1$ Wilson-clover twisted-mass fermions*, *Phys. Rev. D* **104** (2021) 074520 [2104.06747].

[93] PACS collaboration, E. Shintani and Y. Kuramashi, *Hadronic vacuum polarization contribution to the muon $g-2$ with 2+1 flavor lattice QCD on a larger than (10 fm)^4 lattice at the physical point*, *Phys. Rev. D* **100** (2019) 034517 [1902.00885].

[94] Fermilab Lattice, HPQCD, MILC collaboration, C. T. H. Davies et al., *Hadronic-vacuum-polarization contribution to the muon's anomalous magnetic moment from four-flavor lattice QCD*, *Phys. Rev. D* **101** (2020) 034512 [1902.04223].

[95] European Twisted Mass collaboration, D. Giusti, V. Lubicz, G. Martinelli, F. Sanfilippo and S. Simula, *Electromagnetic and strong isospin-breaking corrections to the muon $g-2$ from Lattice QCD+QED*, *Phys. Rev. D* **99** (2019) 114502 [1901.10462].

[96] Muon $g-2$ collaboration, G. W. Bennett et al., *Final Report of the Muon E821 Anomalous Magnetic Moment Measurement at BNL*, *Phys. Rev. D* **73** (2006) 072003 [hep-ex/0602035].

[97] M. Hayakawa and S. Uno, *QED in finite volume and finite size scaling effect on electromagnetic properties of hadrons*, *Prog. Theor. Phys.* **120** (2008) 413 [0804.2044].

[98] RM123 collaboration, G. M. de Divitiis, R. Frezzotti, V. Lubicz, G. Martinelli, R. Petronzio, G. C. Rossi et al., *Leading isospin breaking effects on the lattice*, *Phys. Rev. D* **87** (2013) 114505 [1303.4896].

[99] A. Risch and H. Wittig, *Leading isospin breaking effects in the HVP contribution to a_μ and to the running of α*, *PoS* **LATTICE2021** (2022) 106 [2112.00878].

[100] A. Risch, *Isospin breaking effects in hadronic matrix elements on the lattice*, Ph.D. thesis, Mainz U., 2021. 10.25358/openscience-6314.

[101] E.-H. Chao, H. B. Meyer and J. Parrino, *Coordinate-space calculation of QED corrections to the hadronic vacuum polarization contribution to $(g-2)_\mu$*, *PoS* **LATTICE2023** (2024) 256 [2310.20556].

[102] V. Biloshytskyi, E.-H. Chao, H. B. Meyer and J. Parrino, *Computing the UV-finite electromagnetic corrections to hadronic vacuum polarisation in the muon $(g-2)$ from lattice QCD*, to be published.

[103] V. Biloshytskyi, E.-H. Chao, A. Gérardin, J. R. Green, F. Hagelstein, H. B. Meyer et al.,

Forward light-by-light scattering and electromagnetic correction to hadronic vacuum polarization, JHEP **03** (2023) 194 [2209.02149].

[104] E.-H. Chao, R. J. Hudspith, A. Gérardin, J. R. Green, H. B. Meyer and K. Ottnad, *Hadronic light-by-light contribution to $(g-2)_\mu$ from lattice QCD: a complete calculation*, Eur. Phys. J. C **81** (2021) 651 [2104.02632].

[105] J. Bijnens and J. Relefors, *Pion light-by-light contributions to the muon $g-2$*, JHEP **09** (2016) 113 [1608.01454].

[106] V. Biloshytskyi, E.-H. Chao, D. Erb, F. Hagelstein, H. B. Meyer, J. Parrino et al., "UV-finite QED correction to the hadronic vacuum polarization contribution to $(g-2)_\mu$." https://conference.ippp.dur.ac.uk/event/1265/contributions/7439/attachments/5627/7348/lattice2024_parrino.pdf, 2024.

[107] A. M. Segner, A. Risch and H. Wittig, *Precision Determination of Baryon Masses including Isospin-breaking*, PoS **LATTICE2023** (2023) 044 [2312.09065].

[108] C. R. Harris, K. J. Millman, S. J. van der Walt, R. Gommers, P. Virtanen, D. Cournapeau et al., *Array programming with NumPy*, Nature **585** (2020) 357.

[109] D. Maclaurin, D. Duvenaud and R. P. Adams, *Autograd: Effortless gradients in numpy*, in *ICML 2015 AutoML Workshop*, vol. 238, p. 5, 2015.

[110] J. D. Hunter, *Matplotlib: A 2d graphics environment*, Computing in Science & Engineering **9** (2007) 90.

[111] T. Williams, C. Kelley and many others, "Gnuplot 4.6: an interactive plotting program." http://gnuplot.sourceforge.net/, April, 2013.

[112] Particle Data Group collaboration, M. Tanabashi et al., *Review of Particle Physics*, Phys. Rev. D **98** (2018) 030001.

[113] A. Bazavov et al., *B- and D-meson leptonic decay constants from four-flavor lattice QCD*, Phys. Rev. D **98** (2018) 074512 [1712.09262].

[114] N. Miller et al., *F_K/F_π from Möbius Domain-Wall fermions solved on gradient-flowed HISQ ensembles*, Phys. Rev. D **102** (2020) 034507 [2005.04795].

[115] S. Borsanyi, S. Dürr, Z. Fodor, C. Hoelbling, S. D. Katz et al., *High-precision scale setting in lattice QCD*, JHEP **1209** (2012) 010 [1203.4469].

[116] T. Blum, *Lattice calculation of the lowest order hadronic contribution to the muon anomalous magnetic moment*, Phys. Rev. Lett. **91** (2003) 052001 [hep-lat/0212018].

[117] Alpha collaboration, B. Blossier et al., *HQET at order $1/m$: II. Spectroscopy in the quenched approximation*, JHEP **05** (2010) 074 [1004.2661].

[118] T. A. DeGrand, *A Conditioning Technique for Matrix Inversion for Wilson Fermions*, Comput. Phys. Commun. **52** (1988) 161.

[119] L. Giusti and M. Lüscher, *Chiral symmetry breaking and the Banks–Casher relation in lattice QCD with Wilson quarks*, JHEP **03** (2009) 013 [0812.3638].

[120] V. Hernandez, J. E. Roman and V. Vidal, *SLEPc: A scalable and flexible toolkit for the solution of eigenvalue problems*, ACM Trans. Math. Software **31** (2005) 351.

[121] J. E. Roman, C. Campos, E. Romero and A. Tomas, *SLEPc users manual*, Tech. Rep. DSIC-II/24/02 - Revision 3.14, D. Sistemes Informàtics i Computació, Universitat Politècnica de València, 2020.

[122] S. Balay, S. Abhyankar, M. F. Adams, J. Brown, P. Brune, K. Buschelman et al., *PETSc users manual*, Tech. Rep. ANL-95/11 - Revision 3.11, Argonne National Laboratory, 2019. 10.2172/2205494.

[123] S. Balay, W. D. Gropp, L. C. McInnes and B. F. Smith, *Efficient management of parallelism in object oriented numerical software libraries*, in *Modern Software Tools in Scientific Computing*, E. Arge, A. M. Bruaset and H. P. Langtangen, eds., pp. 163–202, Birkhäuser Press, 1997, 10.1007/978-1-4612-1986-6_8.

[124] M. Lüscher, *Local coherence and deflation of the low quark modes in lattice QCD*, *JHEP* **07** (2007) 081 [0706.2298].

[125] M. Lüscher and S. Schaefer, "openQCD." http://luscher.web.cern.ch/luscher/openQCD/.

[126] ETM collaboration, P. Boucaud et al., *Dynamical Twisted Mass Fermions with Light Quarks: Simulation and Analysis Details*, *Comput. Phys. Commun.* **179** (2008) 695 [0803.0224].

[127] G. S. Bali, S. Collins and A. Schäfer, *Effective noise reduction techniques for disconnected loops in Lattice QCD*, *Comput. Phys. Commun.* **181** (2010) 1570 [0910.3970].

[128] T. Blum, T. Izubuchi and E. Shintani, *New class of variance-reduction techniques using lattice symmetries*, *Phys. Rev. D* **88** (2013) 094503 [1208.4349].

[129] C. Michael and I. Teasdale, *Extracting Glueball Masses From Lattice QCD*, *Nucl. Phys. B* **215** (1983) 433.

[130] M. Lüscher and U. Wolff, *How to Calculate the Elastic Scattering Matrix in Two-dimensional Quantum Field Theories by Numerical Simulation*, *Nucl. Phys. B* **339** (1990) 222.

[131] ALPHA collaboration, B. Blossier, M. Della Morte, G. von Hippel, T. Mendes and R. Sommer, *On the generalized eigenvalue method for energies and matrix elements in lattice field theory*, *JHEP* **04** (2009) 094 [0902.1265].

[132] ALPHA collaboration, B. Blossier, M. Della Morte, N. Garron, G. von Hippel, T. Mendes, H. Simma et al., *HQET at order 1/m: III. Decay constants in the quenched approximation*, *JHEP* **12** (2010) 039 [1006.5816].

[133] E. T. Neil and J. W. Sitison, *Improved information criteria for Bayesian model averaging in lattice field theory*, *Phys. Rev. D* **109** (2024) 014510 [2208.14983].

[134] F. Erben, J. R. Green, D. Mohler and H. Wittig, *Rho Resonance, Timelike Pion Form Factor, and Implications for Lattice Studies of the Hadronic Vacuum Polarisation*, *Phys. Rev. D* **101** (2020) 054504 [1910.01083].